Tire-Road Friction Coefficient Estimation Using a Multi-scale, Physics-based Model

Eric Wade Peterson

Thesis submitted to the Faculty of the Virginia Polytechnic Institute and State University in partial fulfilment of the requirements for the degree of

Master of Science

in

Mechanical Engineering

Saied Taheri, Chair
Corina Sandu
Tomonari Furukawa

August 26th, 2014
Blacksburg, Virginia

Keywords: Tire Friction, Friction Modeling, Persson Model

Tire-Road Friction Coefficient Estimation Using a Multi-scale, Physics-based Model

Eric Wade Peterson

Abstract

The interaction between a tire and road surface is of critical importance as the motion of a car in both transient and steady-state maneuvers is predicated on the friction forces generated at the tire-road interface. A general method for predicting friction coefficients for an arbitrary asphalt pavement surface would be an invaluable engineering tool for designing many vehicle safety and performance features, tire design, and improving asphalt-aggregate mixtures used for pavement surfaces by manipulating texture. General, physics-based methods for predicting friction are incredibly difficult, if not impossible to realize—However, for the specific case of rubber sliding across a rough surface, the primary physical mechanisms responsible for friction, notably rubber hysteresis, can be modeled.

The objective of the subsequent research is to investigate one such physics model, referred to as Persson Theory, and implement the constitutive equations into a MatLab® code to be solved numerically. The model uses high-resolution surface measurements, along with some of the physical properties of rubber as inputs and outputs the kinetic friction coefficient. The Persson model was successfully implemented into MatLab® and high resolution measurements (from optical microscopy and imaging software) were obtained for a variety of surfaces. Friction coefficients were calculated for each surface and compared with measured friction values obtained from British Pendulum testing. The accuracy and feasibility of the Persson model are discussed and results are compared with a simpler, semi-empirical indenter model. A brief discussion of the merits and drawbacks of the Persson model are offered along with recommendations for future research based on the information acquired from the present study.

Dedication

To my family, friends, and teachers for their continued and completely underserved support.

Acknowledgements

First and foremost, I would like to express my sincerest gratitude to Dr. Saied Taheri for allowing me to work under his guidance alongside my esteemed colleagues at CenTiRe and for giving me the incredible opportunity to study abroad and expand both my cultural horizons and technical knowledge. I would also like to thank Dr. Corina Sandu and Dr. Tomanari Furukawa for agreeing to serve on my thesis committee and the Virginia Tech faculty for their excellent courses, in particular Al Wicks and Pablo Tarazaga.

I would like to thank Mihn-Tan Do for his advice and guidance during my stay in Nantes as well as the numerous other researchers and faculty at IFSTTAR for their wonderful hospitality and invaluable help.

I would also like to thank my colleague Mehran Motamedi for his continual feedback and advice, Dr. Pierrick Legrand for generously and readily donating his time to meet and share constructive insight, and Dr. Bo Persson for his prompt responses to my frequent and abundant questions.

Finally, I would like to thank my friends and family for their constant support.

Table of Contents

List of Symbols

a_T	Frequency Shift Factor	--
A	Area	m^2
c	Specific Heat Capacity	*J/(kg K)*
C	Surface Power Spectral Density (PSD)	m^4
C_{1D}	One-Dimensional PSD	m^3
C_{2D}	Two-Dimensional PSD	m^4
$\bar{C}_{2D}$	Radially-Averaged Two-Dimensional PSD	m^4
D	Thermal Diffusivity	$J/(m^3\ K)$
D_f	Fractal Dimension	--
E	Viscoelastic Modulus	*Pa*
F_f	Friction Force	N
F_N	Normal Force	N
h	Height	*m*
H	Hurst Exponent	--
P	Normalized Apparent-to-Real Contact Area Ratio	--
q_x	Wavevector (x-direction)	*rad/m*
q_y	Wavevector (y-direction)	*rad/m*
$\mathbf{q}$	Wavevector $[q_x, q_y]$	[*rad/m, rad/m*]
q	Wavevector Magnitude	*rad/m*
q_0	Lower Wavevector Cut Off	*rad/m*
q_1	Upper Wave Vector Cut Off	*rad/m*
$\dot{Q}$	Heat Transfer Rate	*W*
R	Macro-asperity Radius	*m*
t_0	One-half Contact Time	*s*
T	Rubber Temperature (local)	*K*
T_0	Ambient temperature	*K*
T_g	Glass Transition Temperature	*K*
T_q	Optimum, Spatially Uniform Temperature	*K*
v	Sliding Velocity	*m/s*
ζ	Magnification	--
λ	Surface Roughness Wavelength	*m*
λ_{th}	Thermal Conductivity	*W/(m K)*
μ	Friction Coefficient	--
ν	Poisson's Ratio	--
ρ	Density	kg/m^3
σ_0	Nominal Normal Pressure	*Pa*
τ	Relaxation Time Constant	*s*
φ	Angle Between Sliding Direction and Wave Vector	*rad*
ω	Perturbation Frequency	*rad/s*

List of Figures

List of Tables

Chapter 1

Introduction

The most important forces governing vehicle dynamics are those generated by the interaction between tires and a road surface. Knowledge of these forces is highly valuable for nearly all facets of vehicle modeling, design, and simulation. The design and effectiveness of many critical safety and performance features common on modern vehicles such as anti-lock braking systems and stability and traction control can be considerably improved with accurate knowledge of the frictional forces at the tire-road interface. Naturally, studying these forces and attempting to model and predict them has been and continues to be the focus of a great deal of research.

Until relatively recently, the predominant methods for friction estimation have been primarily empirically based and require extensive testing to accurately describe friction over a range of environmental conditions. Recent developments in contact theory coupled with technological improvements in optics and profilometry, which make high-resolution measurements of pavement surface topography readily available, have shifted the focus of many researchers to physics-based models that can predict friction for a variety of conditions without the need for expensive and time-consuming empirical tests. Studies in rough surface contact theory have shown that most rough surfaces, including asphalt roads, are fractal, and thus exhibit roughness over a wide range of magnification levels. [22, 23] Friction is influenced not only by the macro texture visible to the naked eye, but also by the roughness that exists down to microscopic scales.

Dr. B.N.J Persson has been at the forefront of this research, developing what many consider to be one the most comprehensive rubber contact and friction models that currently exists. The model, referred to as the Persson Theory, is physics-based, precluding the need for empirical data and takes into account the contributions to friction from every relevant scale.

1.1 Motivation

The interaction between a tire and a road surface is quite complex and friction forces can vary depending on the road surface, surface conditions such as moisture or contamination, and ambient temperature. Most tire friction models currently being used are either simplified, and thus do not account for many of these factors, or they are based on empirical data, and may only be valid for the conditions at which the empirical data was taken. A physics-based model that can accurately predict friction for a variety of road surfaces and conditions would be an invaluable tool for improving tire design and vehicle performance, as well as provide a basis for improving asphalt mixtures for pavement roads to achieve optimal friction characteristics.

1.2 Objective

The objective of the research presented in this study is to implement the constitutive equations of the physics-based friction model into a MatLab® code to numerically evaluate the friction coefficient for given measured road profiles. The model should be able to accurately predict friction for a variety of surfaces and range of environmental conditions, specifically temperature and water effects. The model created through this study should serve as an excellent foundation for predicting tire-road friction forces for different tires and road surfaces in a general way, minimizing the time and costs associated with empirical friction tests.

1.3 Research Approach

The methodology followed in order to achieve the research is defined by the following steps:

1. Extensively review physics-based contact and friction modeling literature, in particular the publications of Dr. Persson.
2. Implement the Persson model into MatLab® for numerical evaluation. A simpler indenter model is also considered and implemented into MatLab® (see Chapter 6), but the primary objective is to implement the Persson model.
3. Verify the Persson model for an idealized surface with predefined surface roughness characteristics. Results for such a surface are readily available in Persson's literature and allow for a quick and easy method to ensure the model has been implemented correctly.
4. Obtain high-resolution measurements for rough surfaces with known, measured surface characteristics. These will serve as the primary inputs for the friction model.
5. Compare the measured friction values with the model results for each surface.
6. Analyze the results and asses the accuracy and reliability of the model and address potential improvements and future work.

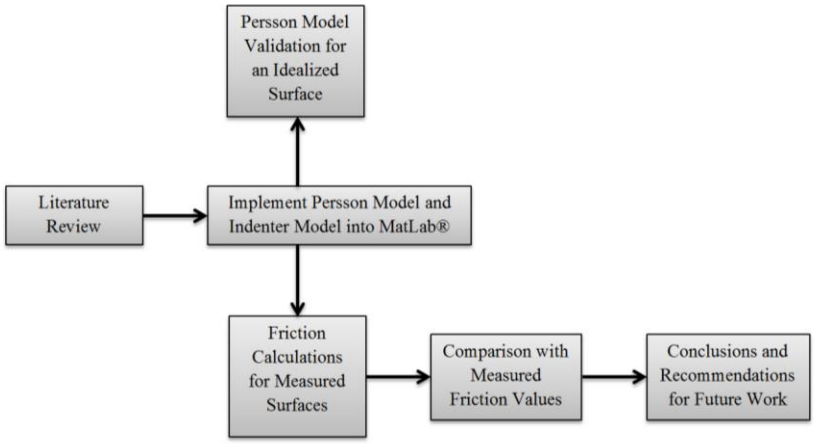

Figure 1.1: Research approach flowchart

1.4 Thesis Outline

A thorough investigation of the challenges and conventional approaches to rubber friction modeling and contact mechanics are offered in Chapter 2 and the Persson Theory is selected as a physics-based model to replicate and validate. Chapters 3 and 4 offer a comprehensive explanation of the constitutive equations used in the Persson Model, how they were implemented into MatLab®, and how water and temperature effects can be incorporated. The model is verified in Chapter 5 for an idealized surface and numerical results are then presented for a variety of rough test surfaces and compared with measured friction values. Chapter 6 offers results obtained from a simpler, indenter model as a point of comparison, and conclusions and suggestions for future work are discussed in Chapter 7.

Chapter 2

Background

2.1 Friction

Friction is generally defined as the force resulting from sliding materials in contact. This phenomenon is present essentially anywhere in nature where there is movement and it is easily observed—without it, it would be impossible for us to drive, walk, or even pick up objects. Scientific descriptions of friction have been recorded as early as the 16th century in the journals of Leonardo da Vinci. Friction theory was independently rediscovered in 1699 by Guillaume Amontons and further developed and expanded throughout the 18th century by many prominent physicists including Charles-Augustin de Coulomb, Leonhard Euler, and John Leslie. Yet, despite its prevalence in nature and the centuries of observation and research, it is only recently that the physical mechanisms that cause friction have really begun to be understood.

Conventional theory for solid bodies states that friction forces are directly proportional to an applied normal load and independent of the apparent contact area. Furthermore, it is observed that the proportionality constant (usually referred to as the friction coefficient, μ) between the normal load and friction force is typically reduced for sliding surfaces, but independent of sliding velocity.

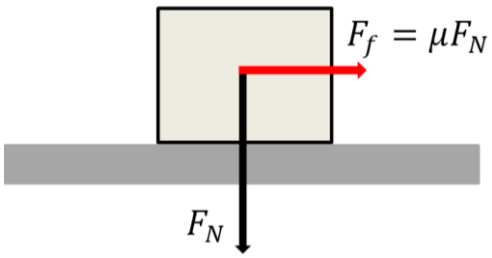

Figure 1.2: Traditional friction model

This theory generally still holds true and is in fact still widely used in engineering. However, it is inexact, as the estimation of friction coefficients is still entirely based on empirical tests. For example, one can easily find a tabulated friction coefficient for rubber and pavement (a typical value might be about 0.7). While this may be a sufficient approximation for some applications, in reality, the actual friction coefficient could vary considerably depending on the asphalt-aggregate mixture, the tire material, temperature, road conditions, speed, etc. A general and practical

method for exactly calculating friction forces between arbitrary surfaces still does not exist, primarily for two reasons:

1. The fundamental forces responsible for friction originate at microscopic and even nanoscopic scales. The technology required to measure or observe forces at such high magnifications is relatively new. Such measurements can be made with an atomic force microscope (AFM), but this technology is quite expensive and not commonly accessible.
2. e in laboratory conditions at such scales are often drastically different from what is observed in a real-world environment. Perhaps the best example of this is the study of diamond friction. Intuitively, one would expect the friction between two diamonds to be relatively low because this is generally what is observed for smooth, hard surfaces. However, in laboratory tests with near-vacuum conditions, the friction coefficient between two diamonds with clean surfaces is actually quite high. The reason for this discrepancy is the presence of very thin contaminant layers that exist in real-world conditions and significantly interfere with the attraction forces at the molecular level (In the case of diamonds, it is a Hydrogen monolayer). [22] While the diamond example may be an extreme case, in reality, most, if not all surfaces will be significantly affected by thin, contamination layers.

Clearly, the calculation of the fundamental forces responsible for friction is an extraordinarily complex problem, and in most cases it is highly impractical, if not impossible to solve. However, in the specific case of tire-road surface interactions, a physical model for friction may be developed due to some of the unique physical characteristics of rubber.

Frictional forces for rubber sliding along a surface are believed to have contributions from two principal physical mechanisms: *adhesion* and *hysteresis*. The hysteresis forces result from energy loss due to internal friction in the rubber as it is deformed by surface asperities. Adhesive forces result from the intermolecular attractions between rubber polymers and a surface (Van der Waals forces). Such forces may be significant for smooth, clean surfaces. However, in the case of tire-road friction, asphalt roads are sufficiently rough and contaminated so that the adhesive forces are widely considered to be negligible. This is quite significant as it changes the scope of the friction-modeling problem from trying to model extremely intricate and multifarious interactions at the atomic level to modeling the deformations and subsequent energy loss of rubber as it slides across a rough surface. The latter problem is still somewhat complex, but it is certainly much more manageable.

2.2 Fractal Nature of Rough Surfaces

Fractals are a fascinating and frequently-studied phenomenon that manifest themselves in a variety of ways in nature. Simply put, a fractal is a mathematical set or geometric pattern that repeats itself on every scale. Common naturally occurring examples of fractal behavior include trees, shorelines, and mountains. It has also been established that surface roughness also exhibits well-defined fractal characteristics [20]. In other words, when one observes a rough surface such as a pavement road, the asperities visible to the naked eye will have smaller asperities on them, and those asperities will be covered with even smaller asperities and so on and so forth. More specifically, rough surfaces are considered to be self-affine fractal, meaning even though asperities exist at different scales, the relative x and y-dimensions do not scale at the same rate. This behavior is described by the fractal dimension D_f or the Hurst exponent: $H = 3 - D_f$. Consequently, the power spectral density of rough surfaces will decay exponentially as a function the Hurst exponent:

$$C(q) \sim q^{-2(H+1)}$$

where C is the power spectral density and q is the wavevector, a frequency variable analogous to ω in the time domain ($q = 2\pi f = 2\pi/\lambda$). Note that the fractal nature is bounded by q_0, the roll-off wavevector, and the short distance cut-off wavevector, q_1. For tire-road applications, q_0 is defined by the largest asperities present—usually the largest stone aggregate used in an asphalt surface and q_1 is dictated by contamination particles such as dust or degraded rubber and is typically on the order of a few micrometers [21]. A more detailed discussion on power spectral densities is offered in Chapter 3.

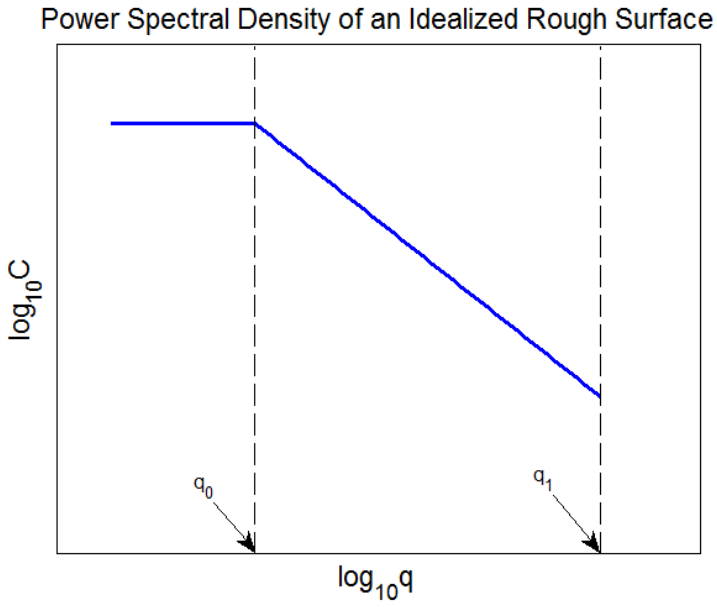

Figure 2.2: Typical PSD behavior for a self-affine fractal surface, fractal for $q_0 \leq q \leq q_1$.

The fact that surface roughness exists over a wide range of scales is extremely important, as any physical friction model must take into account perturbations caused by asperities at each relevant scale.

2.3 Contact Mechanics Models

In order to physically model how rubber is perturbed by surface asperities, it is necessary to physically model the contact. It is widely known (and somewhat intuitive) that the real area of contact between two rough surfaces is relatively small. Additionally, the fractal nature of rough surfaces has significant implications for contact mechanics theories as any contact model must take into account contact on range of scales.

One of the earliest solid contact mechanic models was developed by Heinrich Hertz (for whom the frequency unit 'Hertz' is named) in the 1880's. Hertz approximated surface roughness as smooth, elastic, spherical asperities. When two spheres are in contact, both will deform in accordance with their respective elastic moduli, and a localized stress field is created which is a function the sphere radii, elastic moduli, and the force holding the surfaces in contact.

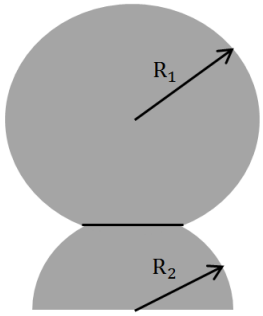

Figure 2.3: Hertz contact theory schematic. The premise for Hertz contact theory is based on representing contacting surface roughness as spherical asperities in elastic contact

Hertz contact theory was an enormous breakthrough in contact mechanics and is in fact still used for a variety of applications including the study of contact forces in many machine elements such as ball bearings and gear meshes. The theory has been expanded for broader applications and advanced to more accurately describe the solid contact phenomenon. For instance, the Greenwood model, which approximates surface asperities as a series of hemispheres varying randomly in size.

Figure 2.4: Surface comprised of hemispheres with randomly distributed diameters. This is the bases for the Greenwood contact theory, and extension of Hertz contact theory.

Still, models based on the Hertz contact theory are not adequate to describe the complex nature of tire-pavement contact. Perhaps the most glaring weakness of many popular contact models is their inability to account for roughness on more than one length of scale.

The contact theory developed by Persson describes contact over a wide range of scales in a physically meaningful way and serves as the basis for the Full Persson Theory.

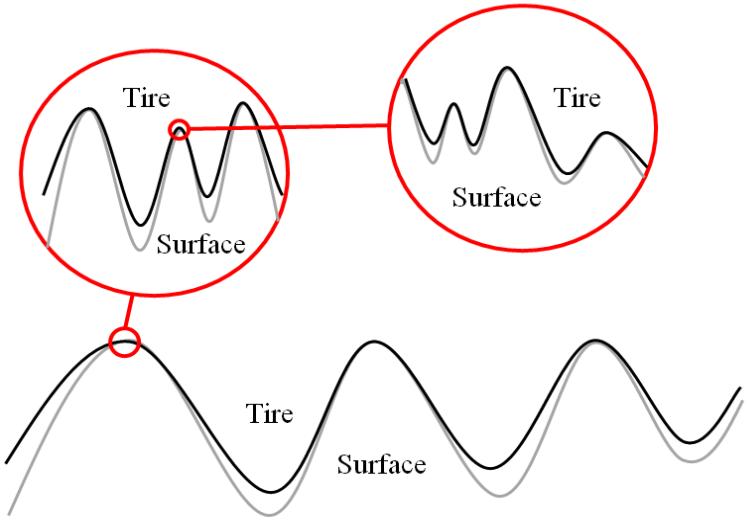

Figure 2.5: Person model schematic, illustrating tire-surface contact. The contact between a tire and rough surface is quite complex because contact isn't maintained throughout the entire roughness profile, and the roughness profiles for multiple lengths of scale must be considered. Persson contact theory accounts for both of these complexities

2.4 Rubber and Viscoelasticity

To understand how energy is lost through hysteresis, it is important to understand the concept of *viscoelasticity*, a property of rubber as well as other soft solids and some non-Newtonian fluids. Many of the most common materials used in engineering applications can be characterized as either solids, which can deform elastically in accordance with their elastic modulus, or (Newtonian) fluids, which exhibit a linear time-dependent resistance to shear deformation in accordance with their viscosity. Rubber is unique in that it exhibits both viscous and elastic effects, hence the term viscoelasticity. Mathematically, the stress-strain relationship for an elastic solid can be described by an extension of Hooke's law:

$$\sigma = E\epsilon$$

where σ is the normal stress, ϵ is the material strain, and E is the elastic modulus—a material constant. For compressible Newtonian fluids:

$$\sigma = \eta \frac{d\epsilon}{dt}$$

where σ is the viscous stress, $\frac{d\epsilon}{dt}$ is the strain rate, and η is the kinematic viscosity.

Viscoelastic materials are susceptible to both kinds of stresses, so the stress-strain relationship is a bit more involved (i.e. it depends on both the strain and the strain rate). For modeling purposes, it is common to use a linear viscoelastic model which can be realized by some combination of linear elastic springs and viscous dampers. For such models, when subjected to sinusoidal loading conditions, the stress and strain equations will also both be sinusoids with identical frequencies, but varying in phase. It is well known from experimentation that the strain will always lag the stress, so, if the time origin $(t = 0)$ is selected at a point where strain is at a maximum $(\epsilon = \epsilon_0)$, stress and strain relationships can be expressed using the following equations:

$$\epsilon = \epsilon_0 \cos(\omega t)$$

$$\sigma = \sigma_0 \cos(\omega t + \delta)$$

Using a different notation common for harmonic systems, the stress equation can be rewritten in terms of real and imaginary components:

$$\sigma^* = \sigma_0' \cos(\omega t) + i\sigma_0'' \sin(\omega t)$$

where $\sigma_0' = \sigma_0 \cos(\delta)$, $\sigma_0'' = \sigma_0 \sin(\delta)$, $\tan(\delta) = \frac{\sigma_0''}{\sigma_0'}$, and $|\sigma^*| = \sigma_0 = \sqrt{(\sigma_0')^2 + (\sigma_0'')^2}$.

Note that the real component of the stress is in phase with the strain and the imaginary component is exactly 90 degrees out of phase with the strain. We can now define moduli as the stress-to-strain ratio for the in-phase and out-of-phase stress components:

$$E' = \frac{\sigma_0'}{\epsilon_0}$$

$$E'' = \frac{\sigma_0''}{\epsilon_0}$$

The result is a complex expression for the stress-strain relationship known as the viscoelastic modulus (sometimes called the complex or dynamic modulus):

$$E = E' + iE''$$

E' is often referred to as the "storage" modulus and E'' is often referred to as the "loss" modulus. There are many different possible spring/damper combinations that can be used for linear viscoelastic models with varying degrees of accuracy and complexity.

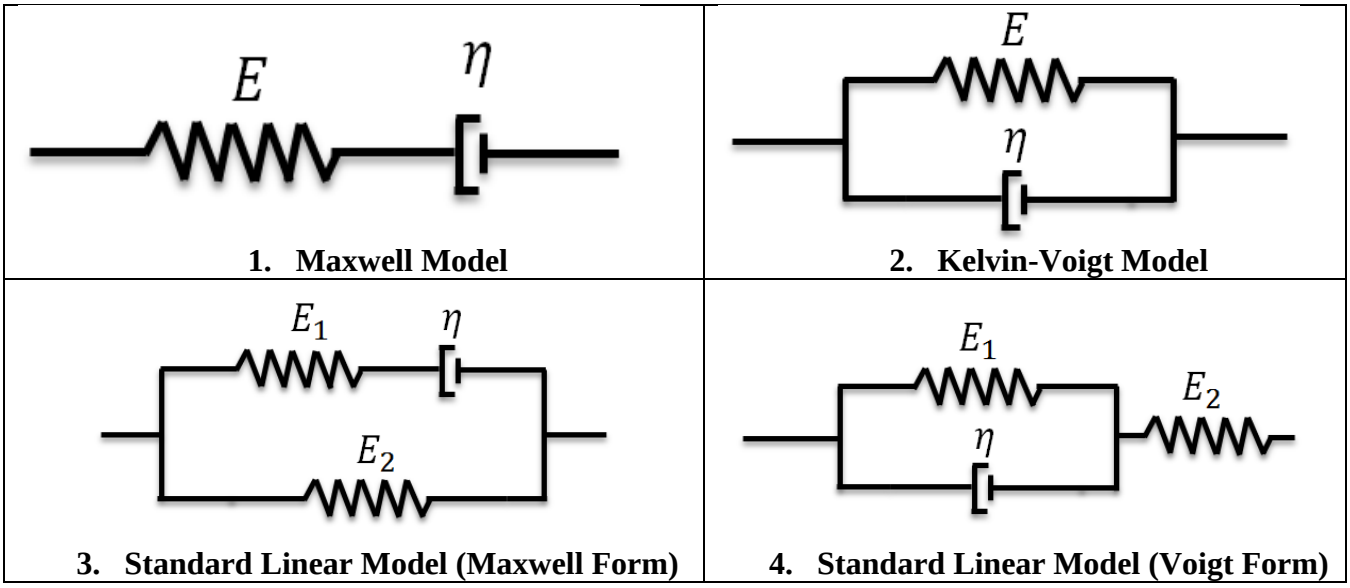

Table 2.1: Commonly used viscoelastic models

For rubber, the Kelvin-Voigt Model and the Voigt form of the Standard Linear Model (SLM) are the most common models utilized. In many of Persson's works, results are presented using the SLM (Voigt form), so this is the viscoelastic model that will be used for the present study.

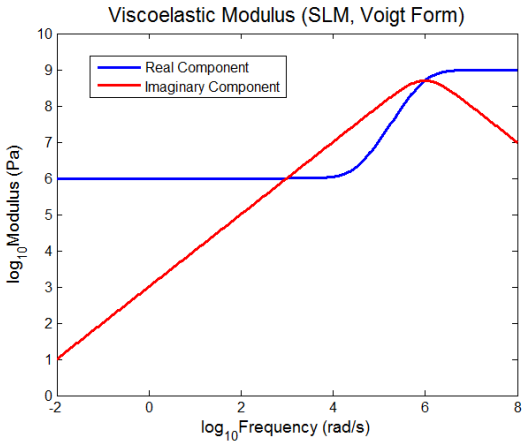

Figure 2.6: Complex viscoelastic modulus for the Standard Linear Model (Voigt Form)

SLM Parameters	
E_1	10^9 Pa
E_2	10^6 Pa
τ	.001 s

Table 2.2: Viscoelastic parameters for the standard linear model. These parameters were taken from Persson's literature and provide a rough approximation of what is typical for tire tread compounds.

2.5 Friction Testing

Extensive testing is required to validate the model and ensure that it is accurate for a variety of road surfaces and conditions. Lab-prepared sample surfaces were prepared and high-resolution profile measurements were taken from each sample for use with the friction model, and the friction coefficient for each sample was found experimentally using the *British Pendulum Test*.

Pendulum tests are frequently used in many applications to measure the energy loss for some mechanical process. The premise is the pendulum, starting from a known height, swings downward through some interaction with a test sample, and up to a new height. Simple energy methods can be used to calculate the energy lost during the swing based on the height the pendulum reaches on its up-swing. In the British Pendulum Test, the bottom surface of the pendulum is a rubber slider, which slides across a prepared surface and the measured energy loss directly corresponds to the friction between the rubber and the test sample.

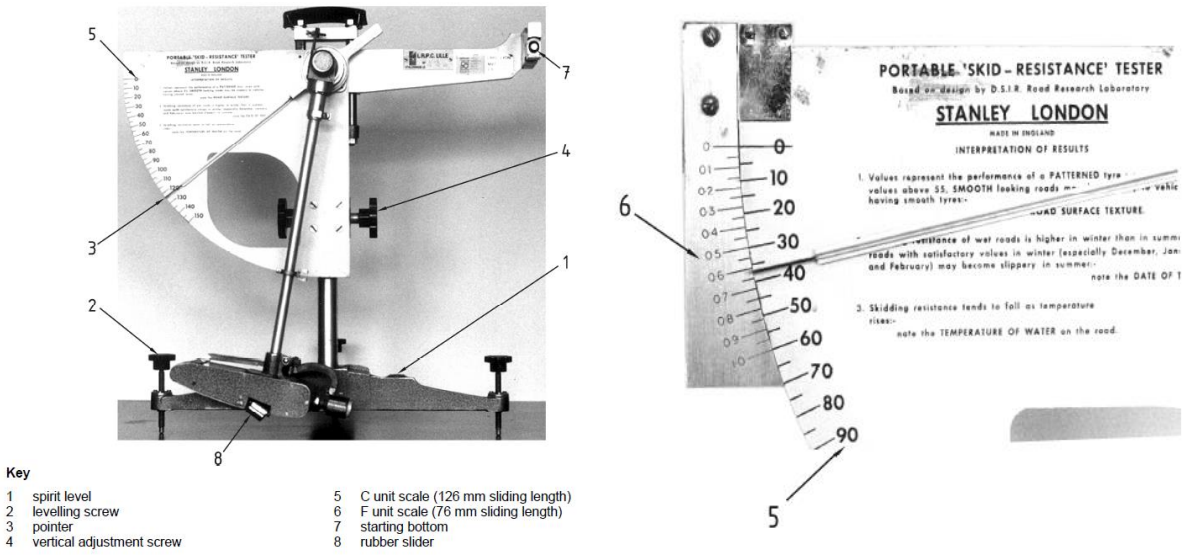

Figure 2.7: British pendulum test apparatus (Technical Committee CEN/TC 227 "European Standard 13036-4. "Method for measurement of slip/skid resistance of surface – Part 4: The pendulum test." 2009. Used under Fair Use, 2014.

The skid-resistance is measured on a circular scale, calibrated for a 126 mm sliding length. The measurement from the scale is a standardized value known as the PTV (Pendulum Test Value) or alternatively, the BPN (British Pendulum Number) and can be converted to a coefficient of friction using the following equation [30]:

$$\mu = \frac{3 \text{ x PTV}}{330 - \text{PTV}}$$

2.6 Data Acquisition

Two basic types of lab-prepared surfaces were analyzed: solid granite surfaces and mosaic surfaces, created by gluing many aggregate particles together in a rectangular pattern (Figure 2.8). Profilometry measurements were taken with an Alicona™ optical microscope and 3D micro-coordinate software. The measurements were taken along lines with a length on the order of 1 cm at 5 different locations along the sample. At each location 4 "lines" of measurement data were recorded, so a total of 20 line scans were taken from each sample. The spatial resolution of the measurements was on the order of one micron.

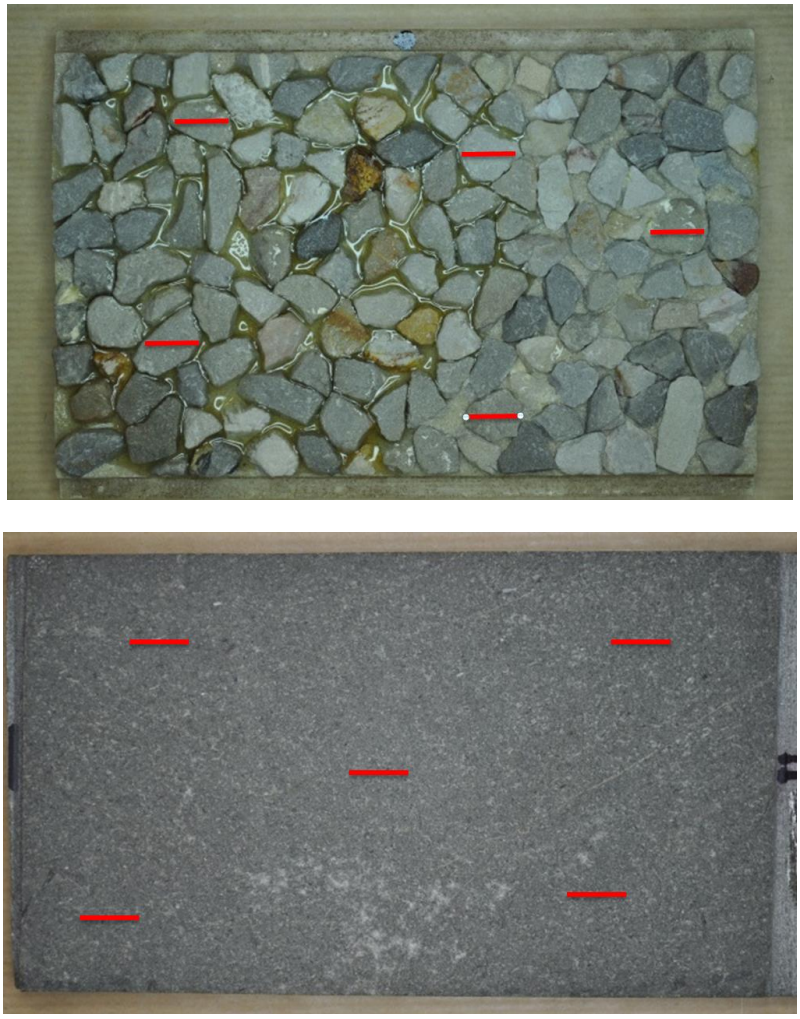

Figure 2.8: Photographs of lab-prepared surfaces that were analyzed. A mosaic surface (top) and granite surface (bottom) are both shown. The red lines indicate locations where measurements were taken from. For the mosaic surfaces, measurements were taken along the flat surfaces of individual aggregate stones.

2.7 Conclusion

A comprehensive literature review of friction modeling has shown that physics-based models have been successful, both quantitatively and qualitatively, in predicting rubber friction for rough surfaces by modeling the rubber deformation and calculating the corresponding energy loss due to hysteresis. The Persson Theory is widely considered to be the most comprehensive model by professionals in both academia and industry and thus was chosen as the model to implement.

The challenges in rubber friction modeling have been addressed, specifically the need for a multi-scale contact mechanics model, such as the one offered by Persson. An explanation of rheological friction models was given and the Voigt form of the Standard Linear Model was selected. Finally, the procedure for friction testing using the British Pendulum Test was established.

Chapter 3

Persson Model Overview

The model developed is based on what is referred to as the Full Persson theory. This theory takes into account the statistical properties of an arbitrarily rough surface texture, the real contact area and its relation to the length of scale, and uses this information to predict rubber deformation and the resulting friction from rubber hysteresis.

The equation developed by Persson for calculating friction coefficient is:

$$\mu = \frac{1}{2}\int d^2q\, q^2 C(q) P(q) \cos(\varphi)\, \mathrm{Im}\left(\frac{E(qv\cos\varphi)}{(1-\nu^2)\sigma_0}\right) \tag{3.1}$$

This chapter does not provide a rigorous mathematical derivation of this equation, but rather offers explanations of each term with a focus on what they physically represent, how they are calculated, and how they relate to each other. Much of the relevant mathematics is included, but the intent is to provide the reader with a clear conceptual understanding of the equation and the tools to replicate the calculations presented in this paper. Additionally, much of the notation Persson uses is not common in the engineering community so an effort will be made to offer alternative notations that may be clearer for readers with an engineering background.

3.1 Roughness Power Spectral Density and the Discrete Fourier Transform

All of the relevant statistical properties of surface roughness can be completely described by the *roughness power spectral density*, $C(q)$. To fully understand the surface roughness power spectral density (PSD), it is first necessary to understand the basics of Fourier analysis, in particular, the *discrete Fourier transform* (DFT). The DFT transforms a non-continuous (i.e. sampled) signal into the frequency domain. Techniques and algorithms for computing the DFT of a signal are very well developed, as it is one of the most important tools used in the very broad field of digital signal processing. While DFT's are often thought of in terms of time-frequency transformations, the mathematics can just as easily be applied for signals sampled in the spatial domain.

The basic premise of Fourier transforms is that any periodic function can be expressed as the summation of sinusoidal waves with varying amplitudes and wavelengths. To illustrate the concept, consider the measured texture profile of a rough surface shown below:

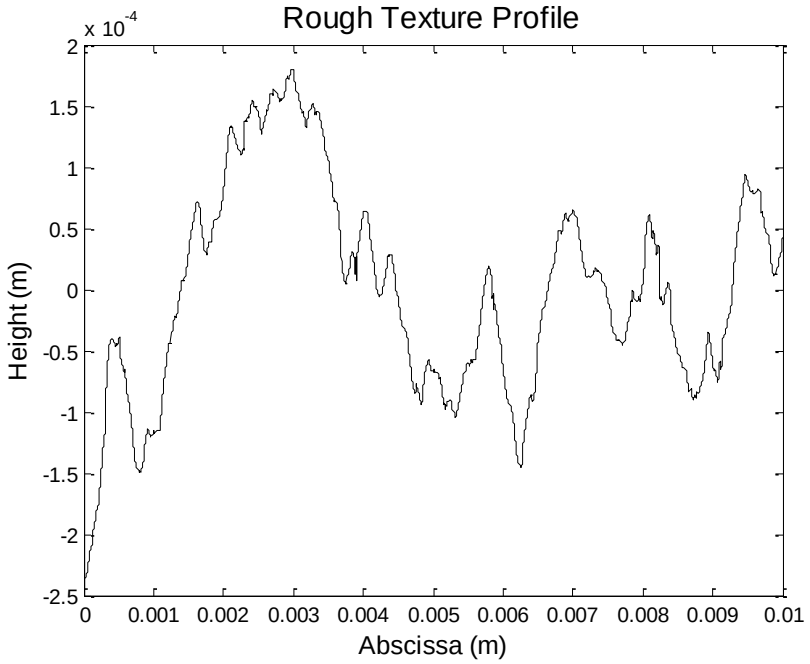

Figure 3.1: Typical 1D line scan measurement of rough surface

By taking the DFT, the signal can be separated into individual frequency components. It is then possible to view the individual sinusoids (in the spatial domain) that are summed to create the original profile by setting all but one frequency component equal to zero and performing the inverse DFT. This is illustrated in the figure below, where approximations are shown using only the first sinusoid, as well as the summation of first 5, 20, and 100 sinusoids:

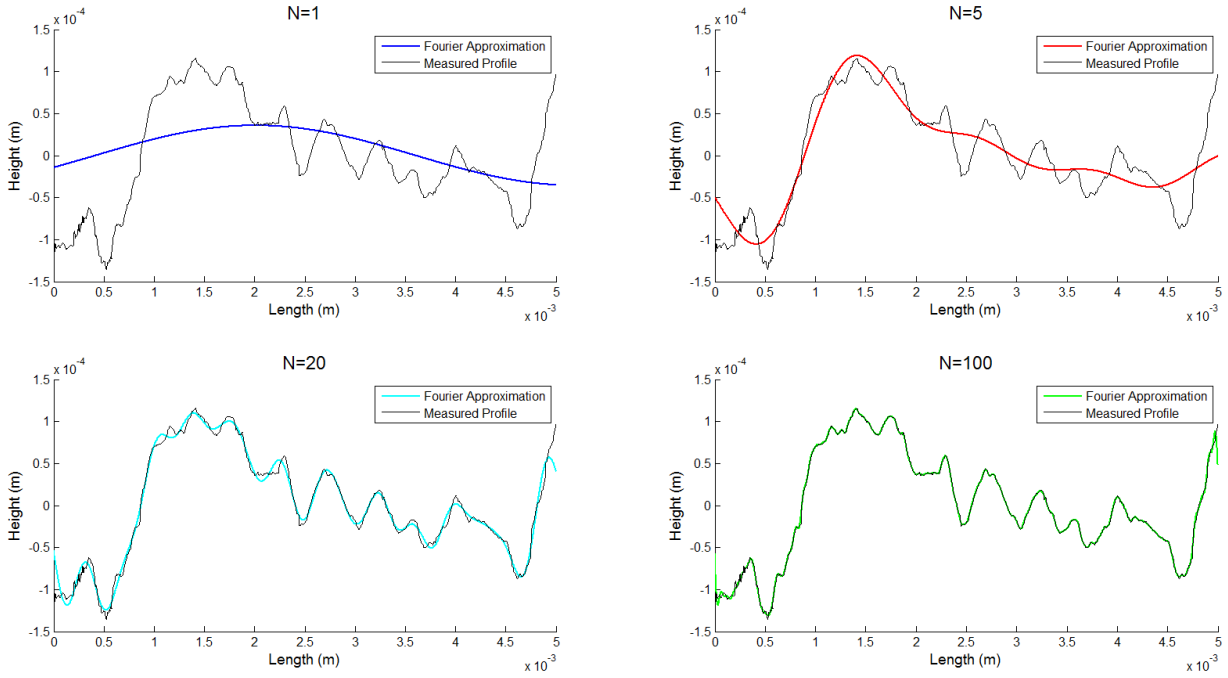

Figure 3.2: Comparison of original measurement with DFT approximations. 'N' denotes the number of DFT terms used to create the approximation.

Note that as more sinusoids are included (with increasing frequency), the smaller asperities are more accurately described by the Fourier series, and the approximation begins to converge to the original measured profile. In fact, when a sinusoid corresponding to every DFT frequency is included, the inverse DFT is an *exact* replication of the original signal. In this case, the DFT was calculated using the Fast Fourier Transform algorithm (FFT), which is by far the most common technique for computing DFTs due to its exceptional computational speed and efficiency.

Persson defines the roughness power spectrum as:

$$C(\mathbf{q}) = \frac{1}{(2\pi)^2} \int d^2x \, \langle h(\mathbf{x}) h(\mathbf{0}) \rangle \, e^{-i\mathbf{q}\mathbf{x}} \tag{3.2}$$

where $h(\mathbf{x})$ is the measured height profile across the x-y plane, $\boldsymbol{x}$, and the brackets $\langle \dots \rangle$ denote ensemble averaging. In words, $C(\mathbf{q})$ is the two-dimensional Fourier transform of the profile's height-height correlation function.

3.1.1 Isotropy and Power Spectral Density Calculations from 1D Line Scan Data

Equation 3.2 is convenient for computing the PSD from two-dimensional data (i.e. when data is measured over an area in both the x and y directions), but in many cases measurement data is only available along a one-dimensional line. Generally, one cannot extrapolate the statistical

information contained in a 1D PSD into two dimensions, however, it can be done if the surface roughness is assumed to be isotropic (i.e. the roughness is uniform in every direction).

Unfortunately, two-dimensional measurement data for a real surface was unavailable for this study, but a randomly rough, isotropic surface with properties similar to those of an asphalt road can be created by using a random number generator to generate a matrix of random numbers, applying a Gaussian filter, and then correlating the filtered and unfiltered matrices. The presence of roughness on a range of scales can be approximated by creating multiple profiles using different standard deviations for the random number generation and different correlation lengths and summing the profiles together. A sample artificially-created surface is shown below:

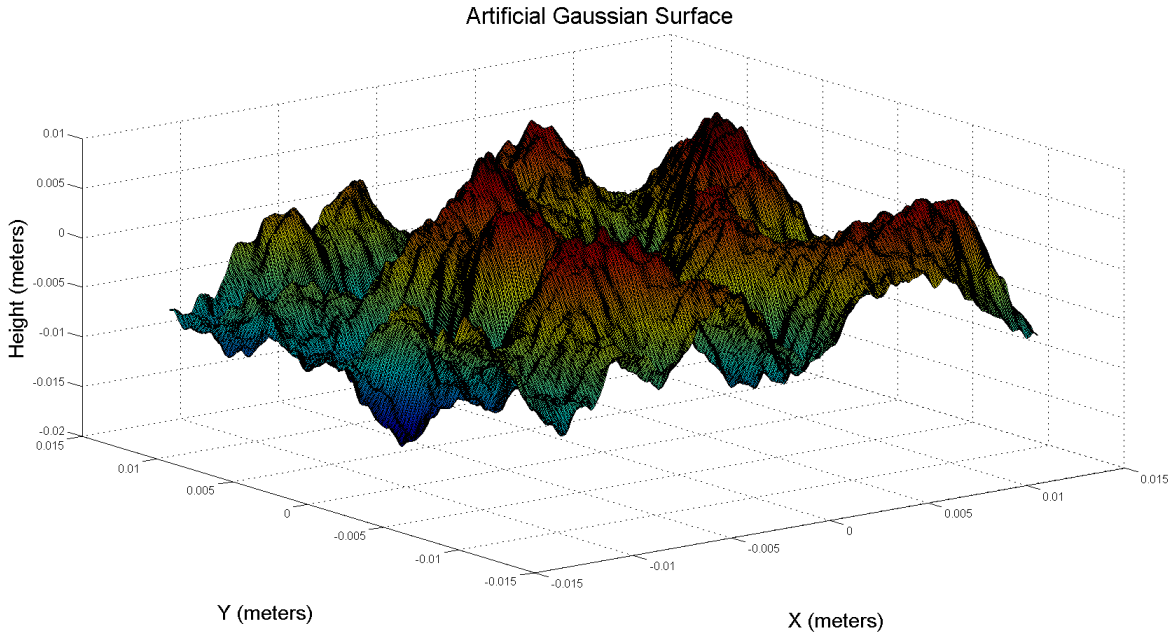

Figure 3.3: Computer-generated isotropic surface

This is admittedly not a perfect approximation of a real randomly rough surface but it is sufficient to provide an example of the 1D to 2D PSD conversion and to prove the validity of the approach. Consider first the two-dimensional PSD of the above surface:

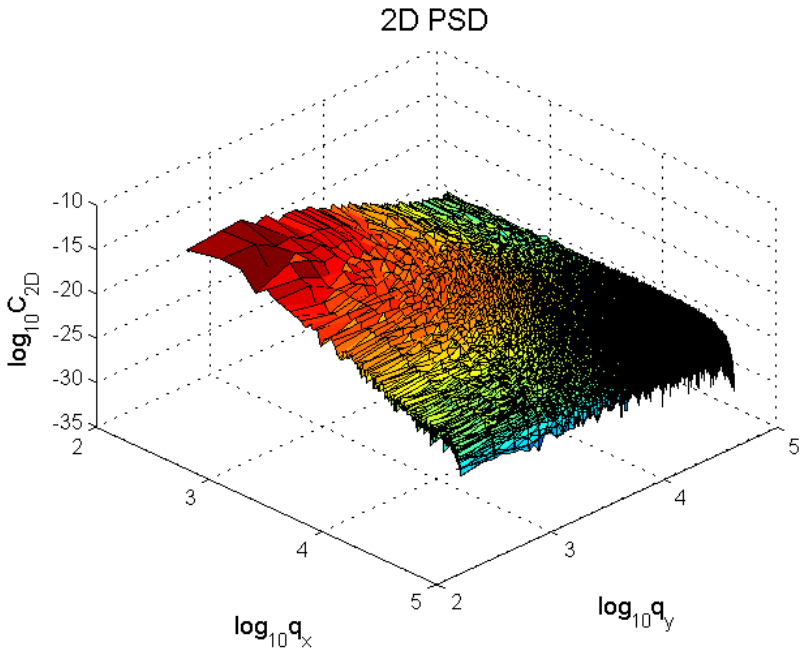

Figure 3.4: Two-dimensional power-spectral density in rectangular coordinates

Note that amplitude of the PSD appears to be independent of the direction of the wave vector **q**. This is consistent with what is expected for an isotropic surface where the following equalities should be observed:

$$C_{2D}(\mathbf{q}) = C_{2D}(q_x) = C_{2D}(q_y) = C_{2D}(q)$$

Since the PSD is only dependent on the magnitude wave vector ($q = |\mathbf{q}|$), it is convenient to view the 2D PSD in polar coordinates and consider only the angular average:

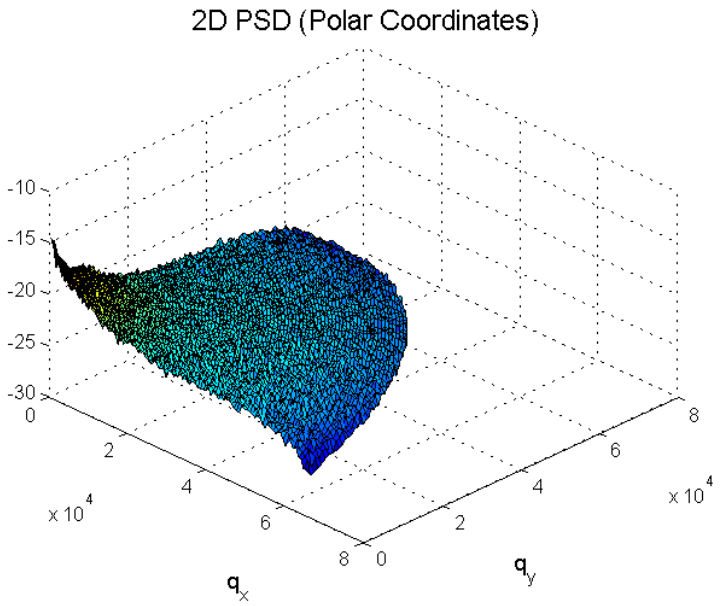

Figure 3.5: Two-dimensional power-spectral density in polar coordinates

Angular Average: $$C_{2D}(q) = \bar{C}_{2D}(q) = \frac{2}{\pi}\int_0^{\frac{\pi}{2}} C_{2D}(q,\varphi)d\varphi$$

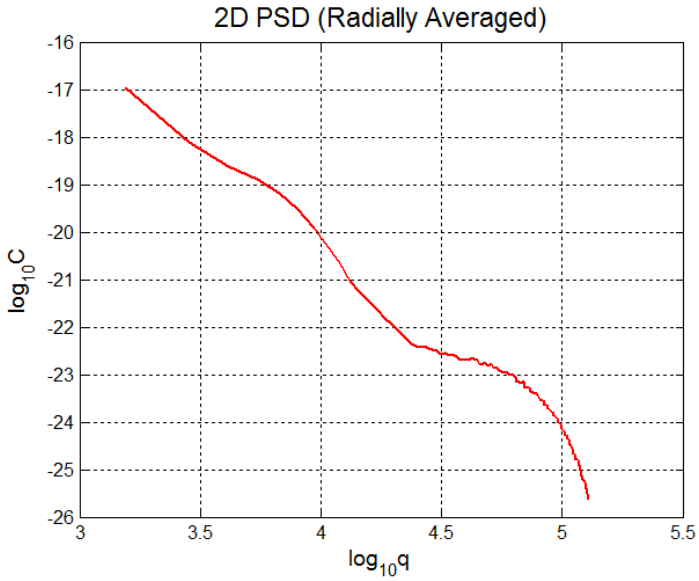

Figure 3.6: Angular averaged two-dimensional power spectral density

Because of the directional independence of the PSD, it is possible to define the 2D PSD in terms of the 1D PSD using the following relationship:

$$C_{2D}(\mathbf{q}) = \delta(q_y)C_{1D}(q_x) \tag{3.4}$$

Furthermore, the angular averages of the two PSD expressions must be equivalent:

$$C_{2D}(q) = \frac{1}{2\pi}\int_0^{2\pi} \delta(q_y)C_{1D}(q_x)d\varphi = \frac{1}{2\pi}\int_0^{2\pi} C_{1D}(q\cos\varphi)\,\delta(q\sin\varphi)d\,\varphi \tag{3.5}$$

After some simplification, a very simple expression for C_{2D} in terms of $C_{1D}$is obtained:

$$C_{2D} = C_{1D}/q \tag{3.6}$$

To verify this technique, it is supposed now that instead of the full 2D surface, only a small sample of 1D cross sections, such as the profile shown below, are available.

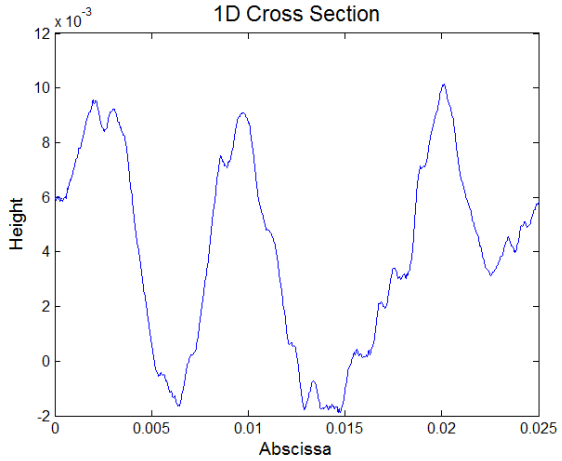

Figure 3.7: One-dimensional profile cross section

The 1D PSD can be computed using a traditional FFT-based algorithm and converted to a 2D PSD using equation 3.5. The 2D PSD of the profile shown in Figure 3.3 was computed using both techniques (converting from 1D PSD and radially averaging the 2D PSD) and the results are plotted together below.

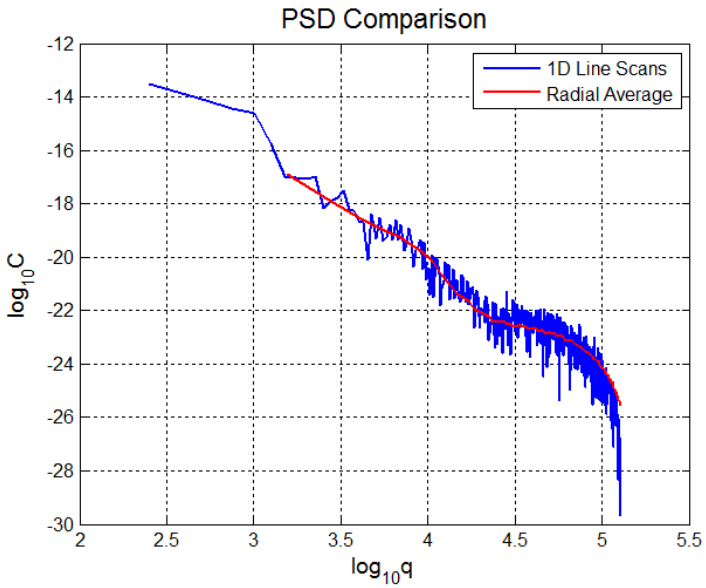

Figure 3.8: PSD calculated using entire 3D profile and 1D cross sections. The blue curve is obtained from cross sections of the profile. The red curve is the angular average of the 2D PSD.

3.2 Real Contact Area

To the naked eye, it would appear that the contract between a tire tread and a road surface is complete. However, experiments have shown that is not the case. In reality, the area of the rubber surface making physical contact with the pavement is disrupted by fractal surface roughness, and is quite small compared with the area of the contact patch (the nominal contact area). This phenomenon is depicted in Figure 3.9, where contact is made at tops of asperities, but the valleys in the surface profile are not quite filled. Generally speaking, at higher levels of magnification, progressively less rubber is contacting the road (this can behavior can be seen graphically in Figure 5.2).

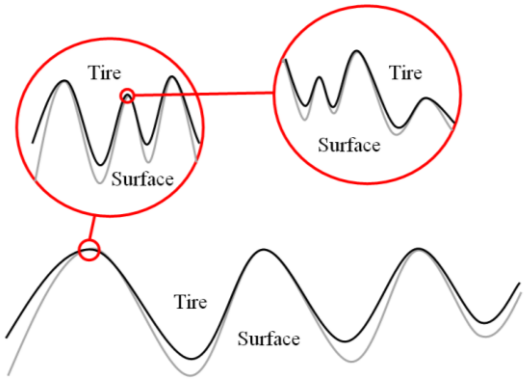

Figure 3.9: Schematic illustrating tire-road surface contact at different levels of magnification. Note that at each level, contact is maintained only at the tops of asperities.

The Persson model accounts for this in a physically meaningful by introducing the term P(q), which is ratio of real contact area to the nominal contact area as a function the wavevector, q. P(q) is given by the following equation:

$$P(q) = (1 + [\pi G(q)]^{3/2})^{-1/3} \tag{3.7}$$

where

$$G(q) = \frac{1}{8}\int q^3 C(q) \int \left|\frac{E(qv\cos(\varphi))}{(1-\nu^2)\sigma_0}\right|^2 d\varphi \, dq \tag{3.8}$$

3.3 Viscoelastic Modulus and Remaining Terms

The rest of the variables used in the Persson equations are physical properties for the tread compound and analysis parameters. E is the rubber's viscoelastic modulus, a frequency dependent and complex quantity which is described in detail in section 2.4. ν is Poisson's ratio, which has a very weak frequency dependence and for tire applications can be assumed to be 0.5. σ_0 is the nominal normal pressure at the tire-road interface and v is the sliding velocity.

It is important to note that many of the same variables, particularly the nominal normal pressure and viscoelastic modulus, are present in both Equation 3.4 and Equation 3.1, the final equation used to calculate the friction coefficient, and they scale inversely. This has an important and perhaps counter-intuitive result: the friction calculated is independent of the nominal normal pressure σ_0 as well as the value of the viscoelastic modulus parameter E_1 (assuming the ratio between E_1 and E_2 is unchanged). In reality, clearly this cannot always be the case, but for tire-road applications for which E_1 is typically much greater than σ_0, it generally holds true.

The algorithm employed to calculate all of the necessary terms is shown in the flowchart in Figure 3.10.

Persson Model Flow Chart

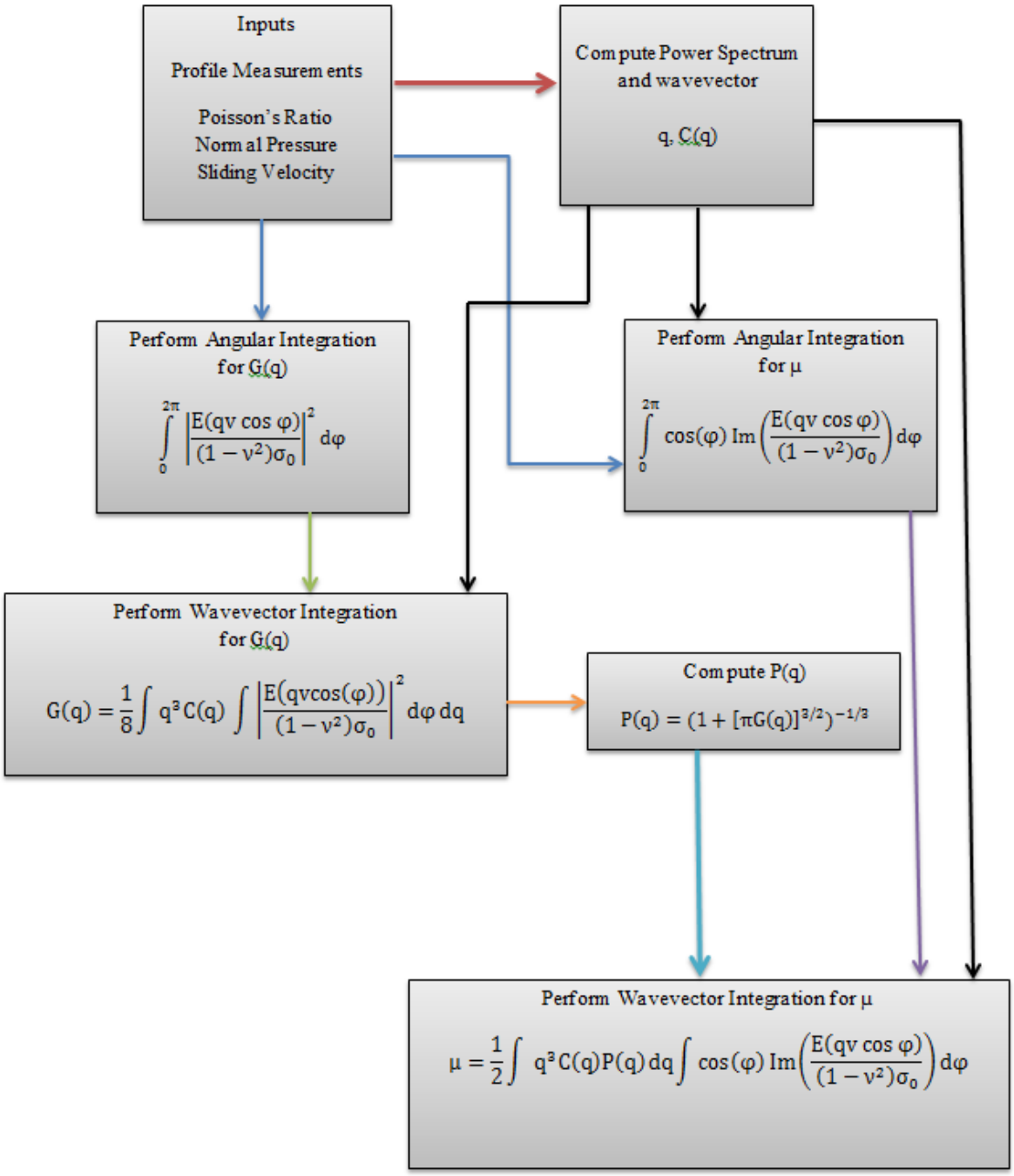

Figure 3.10: Numerical Persson model flow chart

Chapter 4

Water and Temperature Effects

The model that has been developed up to this point assumes road surfaces are dry, and neglects any temperature-induced changes in the viscoelastic modulus. In reality, the viscoelastic modulus of rubber is strongly temperature dependent, and this effect must be accounted for.

Additionally, It is well known that friction coefficient decreases significantly (20-30%) when roads become wet. The full range of effects caused by moisture are very complex and not easily modeled, but one effect that can easily be implemented is the masking of surface asperities, particularly in the profile valleys. This is a good way to physically describe one way water decreases friction in wet friction applications, but is a rather simplistic and does not account for more complex phenomenon such as hydroplaning.

The subsequent sections outline how temperature and moisture affects are implemented added to the model flash temperature and the sealing effect.

4.1 The Sealing Effect

The *sealing effect* provides an effective yet simple way to predict how friction changes for wet roads. Since the model is only taking in to account hysteretic friction, the modification necessary to predict friction on wet roads is very straight-forward. When a road is wet, water will pool in the valleys of the road surface, masking some of the asperities, effectively changing the profile that is "seen" by the tire. This is very easy to incorporate into the model developed in the previous chapter. A fairly simple algorithm can be employed to effectively fill the valleys of a profile, creating a new masked profile. The power spectrum of the new profile can then be computed and the Persson model equations can be used in exactly the same manner as previously described for dry profile measurements.

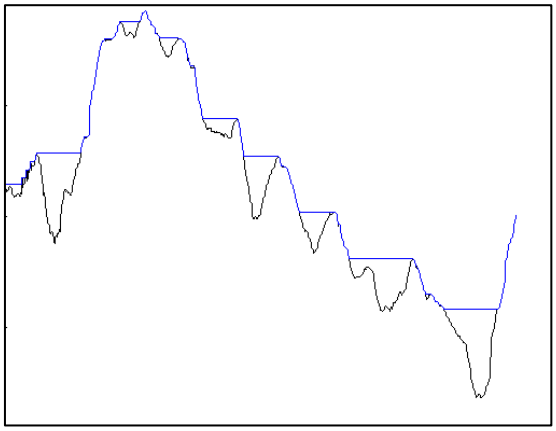

Figure 4.1: Sample profile with valleys 'masked', illustrating the sealing effect

4.2 Flash Temperature

It has been established that in rubber friction applications in which hysteresis is the dominant component (as is believed to be the case for tire-road interactions), the friction forces are predominantly a function of the rubber's viscoelastic modulus, a bulk material property. However, this property is heavily temperature-dependent, so one would expect friction to vary appreciably with changes in temperature. This is indeed the case, and temperature effects must be implemented into the model to account for this.

Modeling the temperature effect on rubber friction can essentially be broken up into two steps: First, the temperature of the rubber at the tire-road interface must be calculated. This will be a function of the ambient temperature and local heat generation within the tire due to frictional energy loss. The temperature increase from local heating at the tire-road interface is referred to as *flash temperature*. Secondly, a temperature-dependent relationship for the viscoelastic modulus must be established so the viscoelasticity of the tire changes appropriately with changes in temperature. These steps are discussed in detail in the next two sections.

4.2.1 The Effect of Temperature on the Viscoelastic Modulus

Williams, Landel, and Ferry have shown that for rubber and many other viscoelastic polymers, changes in temperature will cause the frequency response of the material to shift horizontally along the frequency axis. This is best illustrated graphically by examining the *loss tangent*, defined as the ratio between the imaginary and real components of the viscoelastic modulus. As the temperature increases, the loss tangent is shifted to the right and vice versa.

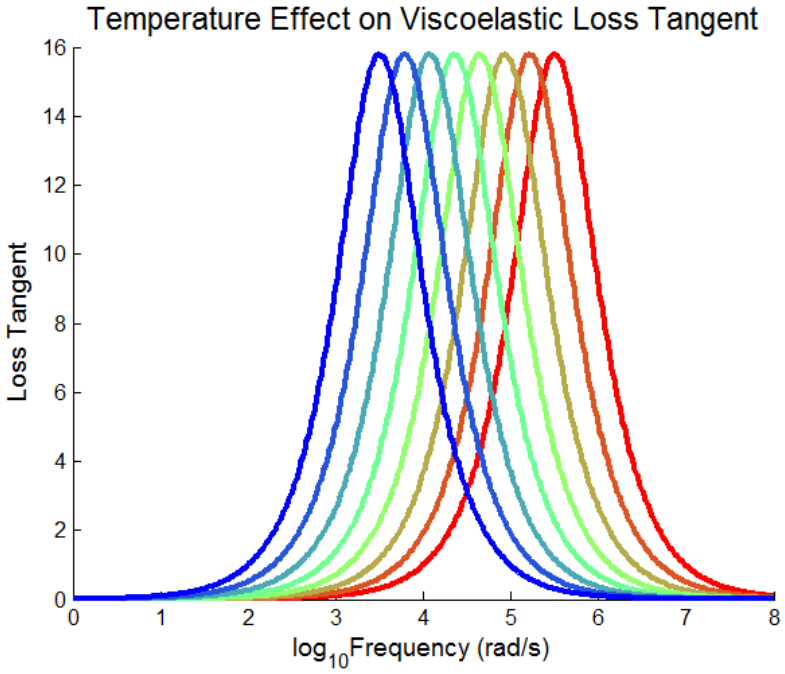

Figure 4.2: Temperature effect on viscoelastic loss tangent

This frequency shift is modeled in an approximate way by using the Williams-Landel-Ferry (WLF) equation to calculate the frequency shift factor:

$$\log_{10}(a_T) \approx -8.86 \frac{T-Tg-50}{51.5+T-T_g} \tag{4.1}$$

where T is the local material temperature and T_g is the glass transition temperature—a material property.

The viscoelastic modulus now becomes a function of the shifted frequency:

$$E(\omega) \rightarrow E(\omega\, a_T / a_{T_0}) \tag{4.2}$$

where a_T and a_{T_0} are the temperature dependent shift factors calculated from equation 4.1 for the local rubber temperature T and the ambient temperature T_0, respectively. In this way, the modeled rubber viscoelasticity becomes dependent on both frequency and temperature.

In theory, the observed frequency shift effect could reduce, increase, or have no effect at all on friction, depending on the range of perturbation frequencies present. The loss tangent is directly related to the energy lost through hysteresis, so friction will be greatest when the rubber is perturbed at a range of frequencies spanning the most of the loss tangent curve. For road-tire applications, the highest frequencies present are nearly always less than ω_0, the frequency corresponding maximum energy loss in the absence of temperature effects. Consequently, for tire-road friction applications one should expect the friction to decrease when the flash temperature effects are included.

4.2.2 Calculating Flash Temperature

White the frequency shift factors obtained from the WLF equation are relatively simple to implement, it is still necessary to calculate the local rubber temperature at the surface interface to use in equation 4.1.

To do this, first consider the heat diffusion equation

$$\frac{\partial T}{\partial t} - D\nabla^2 T = \frac{\dot{Q}(x,t)}{\rho c} \tag{4.3}$$

This equation can be combined with the contact model and expanded to describe temperature variation at different lenghts of scale. The temperature is ‘laterally smeared’ to obtain an effective bulk temperature for the tire tread rubber compounds using equation 4.4:

$$T_q = T_0 + \int_0^\infty g(q,q')f(q')\,dq' \tag{4.4}$$

where

$$f(q) = \frac{vq^4}{\rho C_v} C(q) \frac{P(q)}{P(q_m)} \int \cos\varphi \, \mathrm{Im} \frac{E(qv\cos\varphi, T_q)}{1-\nu^2} d\varphi \tag{4.5}$$

and

$$g(q,q') = \frac{1}{\pi}\int_0^{\infty} \frac{1}{Dk^2}(1 - e^{-Dk^2 t_0}) \frac{4q'}{k^2+4q'^2} \frac{4q}{k^2+4q^2} dk \tag{4.6}$$

Note that now the viscoelastic modulus is a temperature-dependent variable, but the temperature used to compute the viscoelastic modulus is also a function of the viscoelastic model. This interdependency requires the temperature to be solved for in an interative manner.

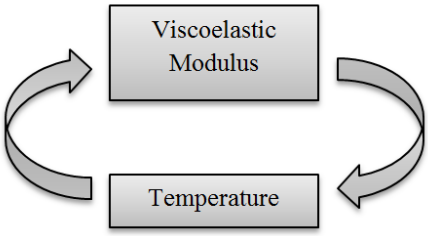

Figure 4.3: Interdependency of viscoelastic modulus and temperature

The algorithm depicted in figure 3.10 must now be amended to iterate until a flash temperature is converged upon. The following set of steps are executed until the temperature converges within some predefined tolerance.

- Guess a starting bulk rubber temperature
- Compute $E(q,T)$
- Compute T_q using equations 4.4 through 4.6
- Use new temperature (T_q) to compute new $E(q,T)$

Once T_q has converged, the temperature is used in the WLF equations to obtain a shifted viscoelastic modulus, and the rest of the model is executed as described in the previous chapter.

Chapter 5

Model Validation and Experimental Results

The constitutive equations that comprise Persson's full friction theory presented in the previous two chapters were implemented into MatLab® to be solved numerically. In this chapter, solutions for an idealized surface are presented and compared to solutions published by Persson to verify that the equations have been implemented correctly. Once this is established, optically-measured profiles of sample surfaces are investigated and the calculated friction coefficients are compared with measured values obtained from British Pendulum Tests.

5.1 Preliminary Comparison for an Idealized Surface

To verify the model has been implemented correctly, it is first compared with results published by Persson for an idealized surface.

A rough surface with the following properties is considered:

q_0	2000 m^{-1}
h_0	0.5 mm
H	0.85

Table 5.1: Idealized surface parameters

where q_0 is the lower cutoff limit of the wave vector q, h_0 is the asperity height with no magnification ($\zeta = 1$), and H is the Husrt exponent. The upper cutoff limit for the wave vector (q_1) can be defined in terms of the magnification, so $q_1 = \zeta q_0$.

The rubber viscoelasticity is modeled using the Voigt form of the Standard Linear as described in 2.4 with parameters $E_1 = 10^9$ Pa, $E_2 = 10^6$ Pa, and τ =0.001 s. Results are obtained for $P(\xi)$ and friction coefficient μ and compared with the same results from literature.

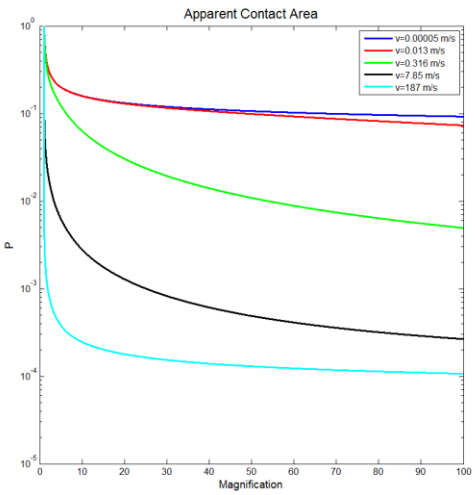

Figure 5.1: Real-to-nominal contact area ratio as a function of magnification, plotted for various sliding velocities

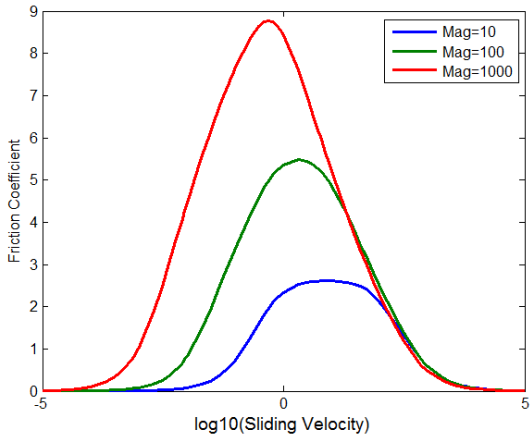

Figure 5.2: Friction coefficient as a function of sliding velocity, plotted for three different magnifications

The numerical results obtained from the MatLab® model appear to be in perfect excellent agreement with what is published in Persson's literature.

5.2 Data Conditioning

Once it has been established that the model has been implemented correctly, measurements of real surfaces are considered. All topography measurements in this study were made with an Alicona™ optical microscope and 3D micro-coordinate measurement software. Measurements were taken as straight-line scans with a length on the order of one centimeter and a spatial resolution of approximately 1 micron (see section 2.6), which should ensure that frequency information for every asperity wavelength contributing to friction is included. The exact measurement parameters vary slightly for different test surfaces, so more detailed descriptions will accompany all of the results presented in subsequent sections.

5.2.1 Outlier Removal

The optical microscopy as the measurement method required minor conditioning before the data can be used with the numerical MatLab® model. First, outliers must be removed. Occasionally, a measurement array may contain a corrupted data point (or points) which appear as a random spikes in the profile. Such anomalies are rare and can easily be removed with a simple algorithm that detects outliers based on the slope at each point along the profile and replaces them with interpolated data.

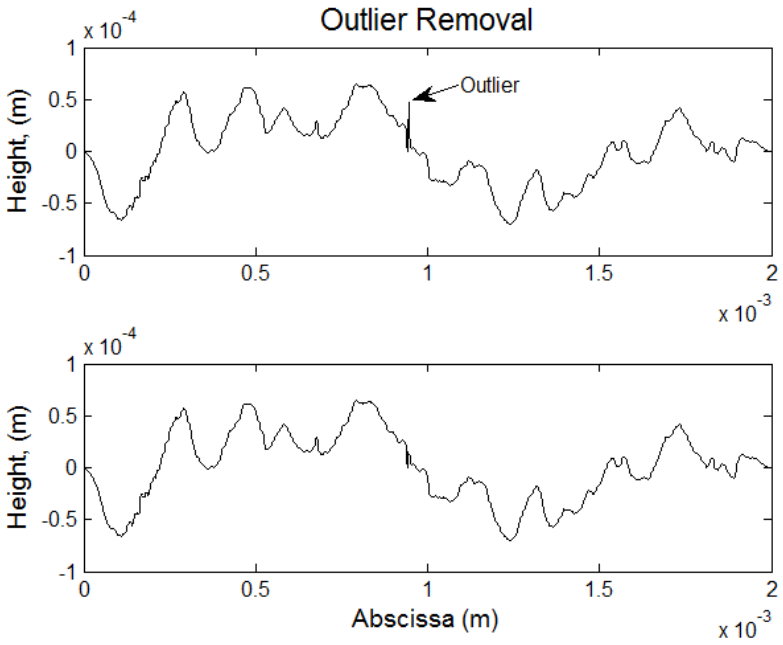

Figure 5.3: Measured profile before and after outlier removal

5.2.2 Resampling and Concatenating Measurement Arrays

Additionally, many of the line scans for a given sample, despite being approximately the same in length and spatial resolution, contained a slightly different number of points. Such measurements can still be used with the numerical model (provided that the DFT for each measurement is the same length), but it is highly advantageous from a computational standpoint to concatenate the measurement arrays for a given test surface to form a single data matrix. To accomplish this, the measurements for each surface are resampled so they are all the same length as the longest measurement. For example, if 20 line scans are taken for a surface, the data matrix used as a model input would be a 20 x N matrix where N is length of the measurement array (typically on the order of 10,000 data points). Note that this will slightly alter the sampling frequency and if the length of two measurement arrays are drastically different, it could have a significant effect on the calculated friction values. However, for relatively small differences (as was the case in this study), the effects are negligible and this technique can greatly improve computational efficiency.

5.2.3 Zero-Mean, Slope Suppression, and Windowing

Zero-mean, slope suppression and windowing are all very common DSP techniques used to slightly modify the original signal with the goal of improving the quality of frequency-domain information.

One of the basic assumptions of discrete Fourier analysis is that the finite measured signal repeats indefinitely as part of an infinitely long periodic function. Obviously, this not truly the case. If one were to stitch multiple profile measurements together to obtain one long, composite profile there would be discontinuities where the end of one profile failed to match with the beginning of the next. However, the profile measurements can essentially be forced to be periodic by applying a window function. A periodic window function is function that begins and ends at zero with a maximum value of unity. By multiplying the original measurement by a window function, the profile is forced to begin and end at zero while the middle of the profile is left unchanged.

There are many types of window functions—each have slightly different shapes and consequently will exhibit different frequency domain characteristics. The Tukey window is an excellent choice for this application, primarily because it attenuates a relatively small portion of the measurement compared with many other windows. The Tukey window is defined mathematically by the following piecewise function:

$$w(n) = \begin{cases} \frac{1}{2}\left[1 + \cos\left(\pi\left(\frac{2n}{\alpha(N-1)} - 1\right)\right)\right] & 0 \le n \le \frac{\alpha(N-1)}{2} \\ 1 & \frac{\alpha(N-1)}{2} \le n \le (N-1)\left(1 - \frac{\alpha}{2}\right) \\ \frac{1}{2}\left[1 + \cos\left(\pi\left(\frac{2n}{\alpha(N-1)} - \frac{2}{\alpha} + 1\right)\right)\right] & (N-1)\left(1 - \frac{\alpha}{2}\right) \le n \le (N-1) \end{cases}$$

where N is the total number of samples and α is a user-defined parameter value between 0 and 1 ($\alpha = 0$ corresponds will yield a rectangular window, which has no effect on the signal, and when $\alpha = 1$, it is equivalent to a Hann window). A Tukey window function ($\alpha = 0.2$), and a windowed profile measurement are plotted below:

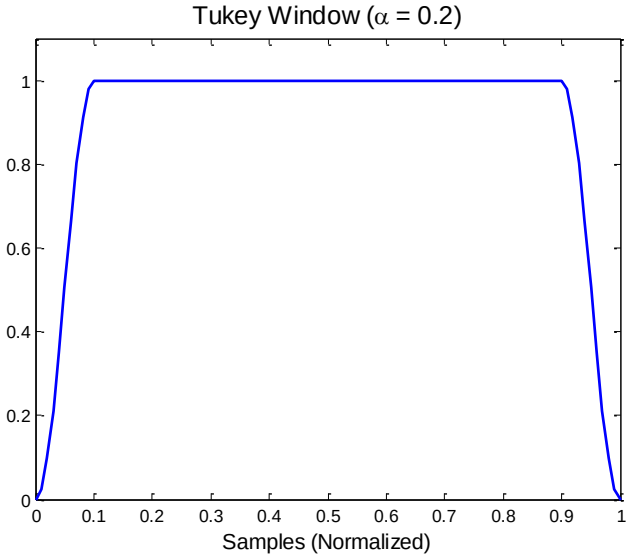

Figure 5.4: Tukey window

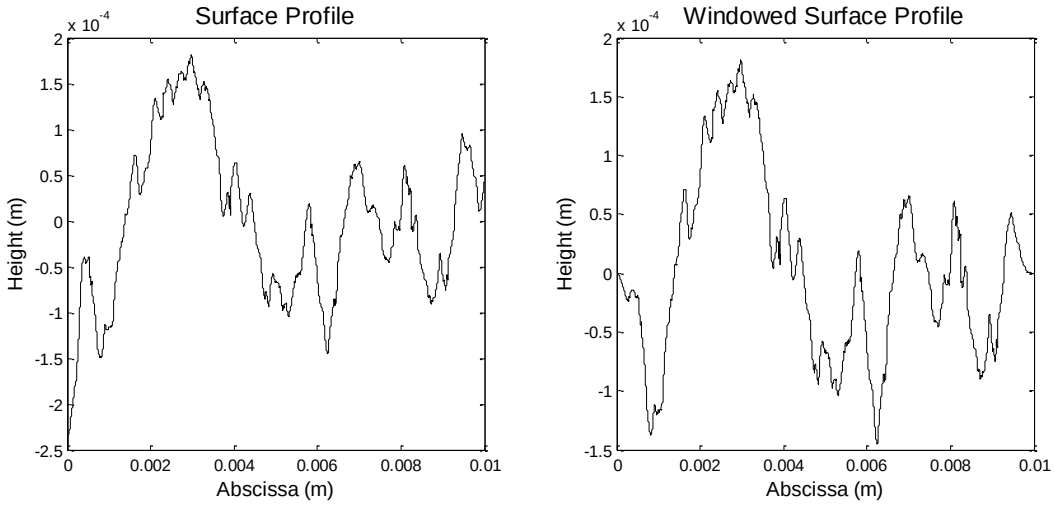

Figure 5.5: Measured profile before and after windowing

5.3 Numerical Results for Granite Surfaces

The first surfaces considered were granite slabs with distinctly different finishes: polished, cut, and sandblasted. These surfaces serve as an excellent starting point for verifying the model because are they have very uniform roughness characteristics, they are easy to measure, and each surface exhibits radically different friction characteristics.

Only three line scans were taken for each surface. Line scans were approximately 1 cm long, with a spatial resolution of about 0.5 micrometers. Initial calculations were made neglecting flash temperature and the sealing effect (the measured friction values are actually for wetted surfaces, as per the standard British Pendulum testing procedures).

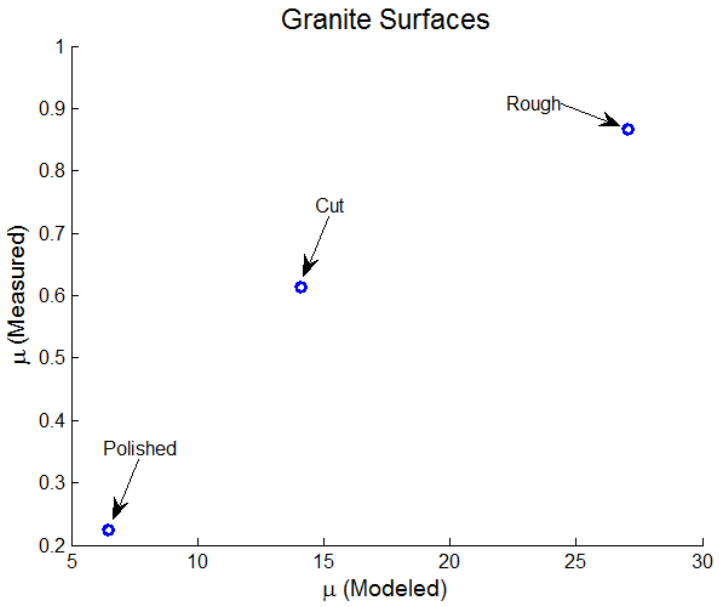

Figure 5.6: Granite surface friction calculations

Figure 5.6 shows excellent qualitative agreement between modeled and measured friction coefficient values, with a nearly linear relationship. However, the model appears to be qualitatively inaccurate. Obviously, a friction coefficient of nearly 30, as calculated for the rough surface, is not realistic. This is actually consistent with some of Persson's numerical calculations with the same rheological viscoelastic model (see Figure 5.2). The standard linear viscoelastic model exhibits a very abrupt rubber-to-glass transition which leads to friction values much higher than what are actually observed. It is likely that better quantitative results could be achieved by using an empirical viscoelastic model, but such data was unavailable. Given the limitations imposed by the viscoelastic model, an excellent qualitative agreement is considered a very satisfactory result.

Calculations were made on the same surfaces with sealing effects included:

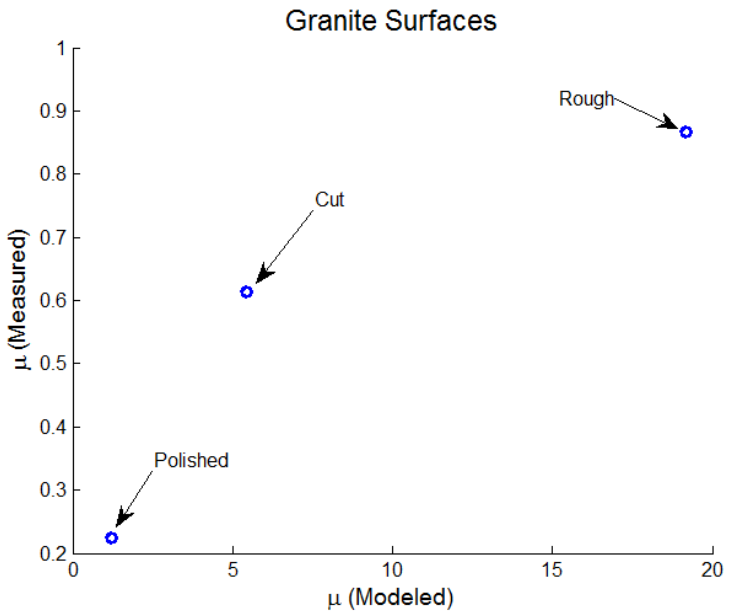

Figure 5.7: Granite surface friction calculations, with temperature and sealing effects included

As expected, the inclusion of the sealing and temperature effect reduces friction considerably and a fairly good qualitative agreement is maintained.

Next, mosaic surfaces are considered. Mosaic surfaces are comprised of stone aggregate, set in adhesive to form a relatively flat, rectangular surface. The line scans were made only on the faces of the aggregate stones.

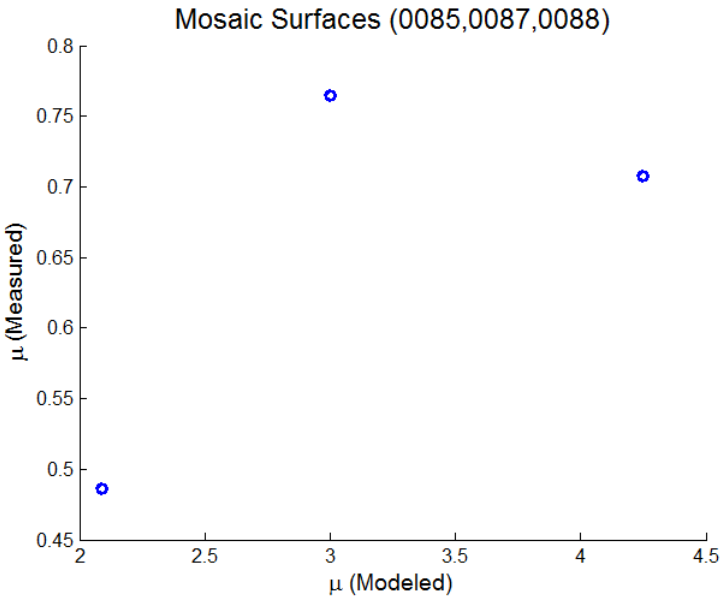

Figure 5.8: Mosaic surface friction calculations

The first three mosaic surfaces yielded a very poor correlation, apparently unable to distinguish even qualitatively between surfaces, especially between two surfaces that had relatively similar friction characteristics.

To better guage the effectiveness for predicting the friction coefficient of the mosaic samples, an additional ten mosaic surfaces were analyzed. The results of all the surfaces (13 mosaic, 3 granite) are plotted in figure 5.7 for a variety of magnification levels and with and without friction and water effects included.

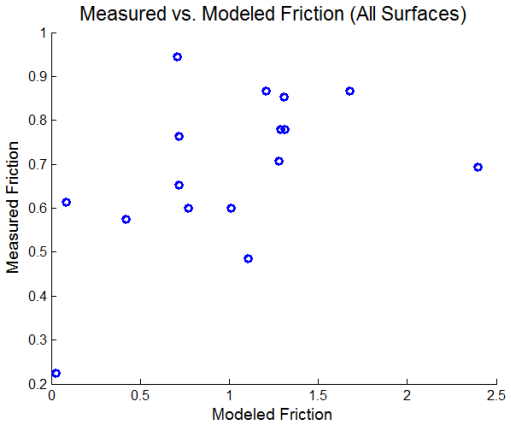

ξ=10, q_0=2000, Water/Temp Effects Neglected

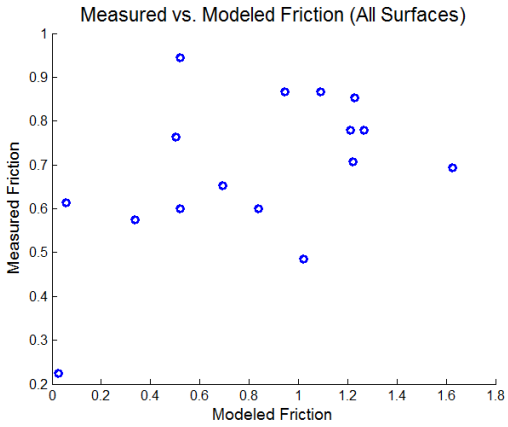

ξ=10, q_0=2000, Water/Temp Effects Included

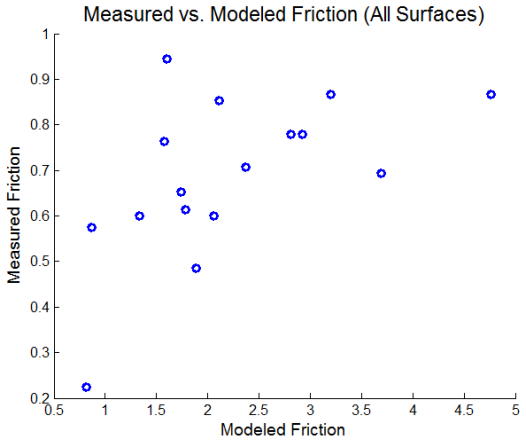

ξ=100, q_0=2000, Water/Temp Effects Neglected

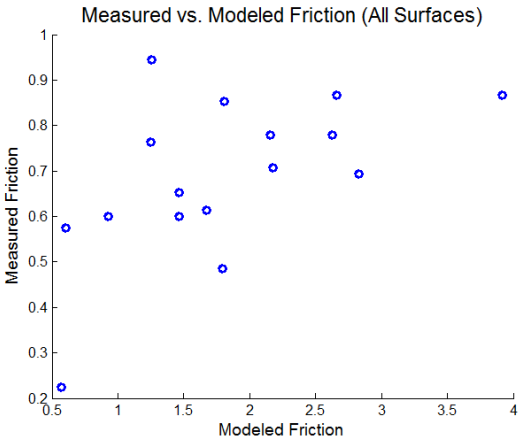

ξ=100, q_0=2000, Water/Temp Effects Included

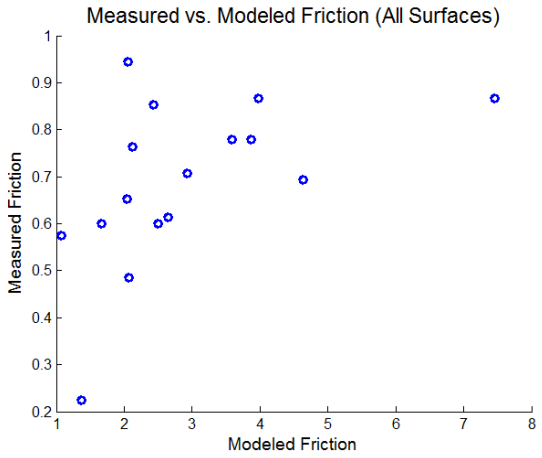

ξ=1000, q_0=2000, Water/Temp Effects Neglected

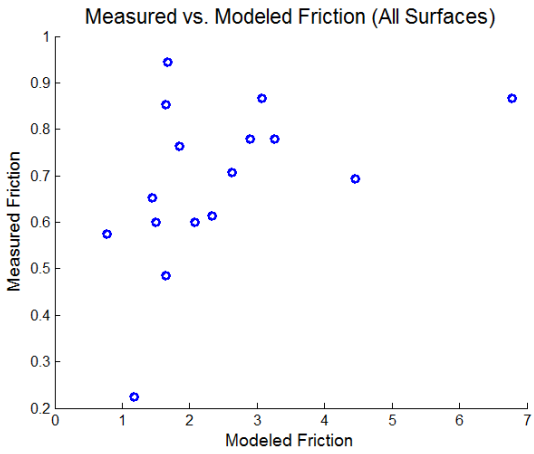

ξ=1000, q_0=2000, Water/Temp Effects Included

Figure 5.9: Measured vs. modeled friction comparison for 16 different surfaces

For an exactly accurate model, one would expect a linear 1:1 relationship between for the plots shown in Figure 5.7. The results are scattered, with a very weak correlation between measured and modeled friction values regardless of the cutoff wavevector value (determined by the magnification, ξ) and temperature and water effects. This discrepancy could potentially be explained by the friction measurement method—the British Pendulum Test is rather primitive and the results may not be definitive. It is certainly conceivable that more comprehensive friction tests with greater reliability and accuracy could yield a better correlation. Additionally, measurements were taken along relatively short sections on the aggregate surface and information about the macro-texture, which could have a significant impact on the BPT results, may have been lost. More homogenous test surfaces which lend themselves better for larger surface measurements could also help to improve results. Still, there is a weak qualitative correlation, especially between surfaces with drastically different textures, and the results are qualitatively about what one would expect, remembering that rheological viscoelastic model employed yields results substantially higher than what is observed in reality.

Chapter 6

Comparison with Indenter Model

6.1 Indenter Model

The Indenter Model is a semi-empirical model which approximates the surface asperities as conical peaks and projects force vectors based on the angles of inclination and declination of the asperity faces.

The forces in the horizontal (x) direction for the ascending and descending faces can be written as functions of the vertical (z) component and the conical peak angle

$$F_{xa} = \frac{F_{za}(\cos\alpha + \mu_0 \sin\alpha)}{\sin\alpha - \mu_0 \cos\alpha} \text{ and } F_{xd} = \frac{F_{zd}(\sin\alpha - \mu_0 \cos\alpha)}{\sin\alpha + \mu_0 \cos\alpha}$$

respectively. The friction coefficient can then be expressed as the ratio of horizontal to vertical forces:

$$\mu = \frac{F_x}{F_z} = \frac{F_{xa} + F_{xd}}{F_z}$$

This can be expanded further by defining $h = F_{za}/F_z$, which is dependent on the material properties of the rubber, specifically the viscoelasticity. The factor h describes the asymmetrical loading of the rubber on the ascending and descending faces (a value of 0.5 would indicate symmetrical loading). In other literature, $h = 0.83$ is a value typical for tire rubbers, and is the value adopted for the all of the subsequent calculations in this section.

Substituting equations 6.1.1, 6.1.2, and the relationship for h into equation 6.1.3, we arrive at the following equation which can be used to calculate the friction coefficient for rubber sliding over a single conical asperity:

$$\mu = h\frac{\cos\alpha + \mu_0 \sin\alpha}{\sin\alpha - \mu_0 \cos\alpha} - (1-h)\frac{\mu_0 \sin\alpha - \cos\alpha}{\sin\alpha - \mu_0 \cos\alpha}$$

The friction coefficient due to rubber deformation can then be computed for a surface profile by applying equation 6.1.4 to each asperity in the measured profile and averaging:

$$\mu_{def} = \frac{F_{x,def}}{F_z} = \frac{1}{N}\sum_{i=1}^{N} \mu_i$$

The effects of water are introduced to the model by assuming some of the asperities are masked by a water layer; this is very similar to the sealing effect described by Persson (see section 4.1). However, this model uses a different algorithm for masking the profiles which introduces the capability of varying the water depth. So, instead of simply categorizing surfaces as wet or dry, we can begin to study, in a simple manner, how friction changes with varying degrees of wetness.

The water depth is defined as the distance from the mean height of profile valleys. It is important to note that when using this convention, it is possible that some asperities may be masked even if the water depth is set to zero.

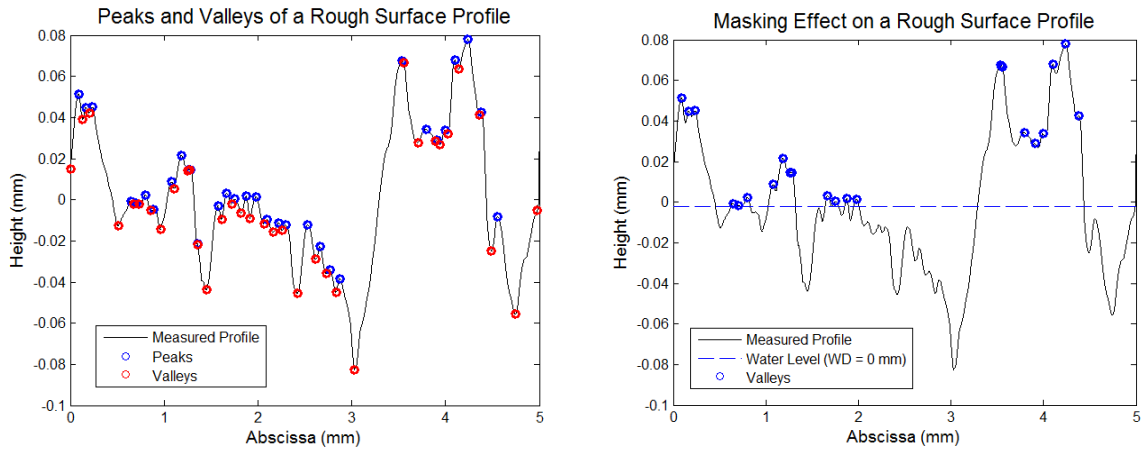

Figure 6.1: The effects of water on surface peaks and valleys in the indenter model. A profile with peaks and valleys identified by the blue and red markers is shown (left) with the same profile with only the peaks above the average valley height marked to illustrate the sealing effect due to moisture.

The model assumes that when no water effects are included the load is uniformly distributed over every asperity. When the masking effect is introduced, the peaks below the water level are assumed to no longer make contact with rubber, but the component of vertical load that they would support under dry conditions is assumed to be supported by the water film.

Mathematically, this can be expressed with a slight amendment to equation 6.1.5:

$$\mu_{\mathrm{def}} = \frac{1}{\mathrm{N}} \sum_{\mathrm{i}=1}^{\mathrm{N}_i} \mu_{\mathrm{i}}$$

where N is still the total number of asperities but the upper bound of the summation is now limited to $\mathrm{N_i}$, the number of asperities above the water level ($\mathrm{N_i} < \mathrm{N}$).

6.2 Indenter Model Results

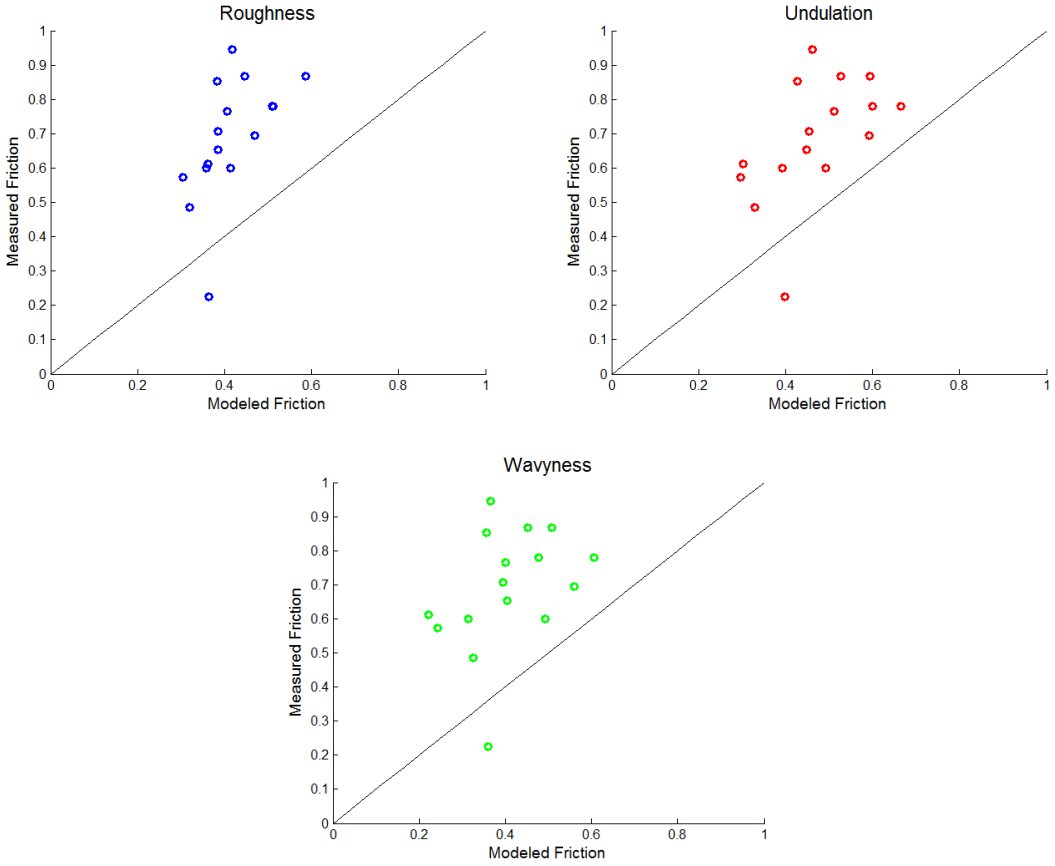

Figure 6.2: Indenter model results for the three scale lengths considered

Again, we notice a relatively weak correlation between measured and modeled friction values which becomes weaker as larger lengths of scale are considered. However, quantitative results are much better. While not exactly correct, they are at least of the correct magnitude for typical friction coefficient values. This method has been shown to be fairly accurate when compared with results to a dynamic friction tester [4] which lends further credence to the idea that poor agreement between modeled and friction values could be due to inaccuracies stemming from the testing methods rather than the model itself.

Chapter 7

Conclusions

The Persson model was successfully implemented into a MatLab® code for numerical evaluation. The results for both apparent-to-real contact area ratio and friction coefficient are in perfect agreement with published results for an idealized surface.

A procedure for calculating the Power Spectral Density of a surface using 1D line scans or measurements over a 2D area was established, and presented in a notation that should be significantly more intuitive for those in the engineering community. The proposed procedure also precludes the need for the use of the complicated inverse able transform offered by Persson in [3].

However, virtually no meaningful correlation was found between measured and modeled friction for the mosaic surfaces studied.

7.1 Recommendations for Future Work

The biggest obstacle to achiever quantitative accuracy is the rheological viscoelastic model, which yields friction results considerably higher than any expectation for realistic conditions (due to the overly abrupt transition from the rubbery to glassy region). This effect could be mitigated by using an empirical viscoelastic model and Persson has shown that using real viscoelastic data yields much more accurate results.

The failure to be able to accurately predict friction for mosaic surfaces, while disappointing, could be explained. The mosaic surface measurements were 0.5 cm in length, and any texture on a scale larger than about 0.25 cm was assumed to be smooth. This assumption likely isn't accurate, as some unevenness at the macro level is easily visible to the naked eye, and could have a significant impact on measured frequency.

Furthermore, the British Pendulum Test may not be exactly accurate. Based on conversations with colleagues with significant knowledge of friction testing, test values can vary considerably depending on the orientation of the surface and are notoriously difficult to replicate.

It is worth noting that the granite surfaces, which are more homogenous and have widely differing friction coefficients form sample to sample, yielded a linear qualitative correlation. For future tests, it is my opinion that asphalt test surfaces should be created in a more homogenous way and different kinematic friction testing methods should be explored.

Bibliography

[1] Abry P, Goncalves P, and Vehel J. *Scaling, Fractals and Wavelets.* Hoboken: John Wiley & Sons, Inc., 2009. PDF.

[2] Bhushan, Bharat. "Contact Mechanics of Rough Surfaces in Tribology: Multiple Asperity Contact." *Tribology Letters* 4 (1998): 1-35. PDF.

[3] Carbone G, Lorenz B, Persson B.N.J., and Wohlers A. "Contact Mechanics and Rubber Friction for Randomly Rough Surfaces With Anisotropic Statistical Properties." *The European Physics Journal E* 29 (2009): 275-284.

[4] Do, Cerezo, Beautru and Kane. "Modeling of the Connection Road Surface Microtexture/Water Depth/Friction." *Wear* 302 (2013): 1426-1435.

[5] Dodds, C.J., and Robson, J.D. "The Description of Road Surface Roughness." *Journal of Sound and Vibration* 31.2 (1973): 175-183.

[6] Fulge, Knapp, et. al. "Improved Abel Inversion Method for Analysis of Spectral and Photo-Optical Data of Magnetic Influenced Plasma Flows." *American Institute of Aeronautics and Astronautics.* 2011.

[7] Heath, A. N., "Application of the Isotropic Road Roughness Assumption." *Journal of Sound and Vibration* 115.1 (1987) PDF.

[8] Heinrich, Gert and Kluppel, Manfred. "Rubber Friction, Tread Deformation and Tire Traction." *Wear* 265 (2008): 1052-1060. PDF.

[9] Kalal, Milan and Nugen, A. "Abel Inversion using Fast Fourier Transforms." *Applied Optics.* 27.10 (1988): 1956-1959

[10] Le Gal A, Yang X, and Kluppel M. "Evaluation of Sliding Friction and Contact Mechanics of Elastomers Based on Dynamic-Mechanical Analysis." *Journal of Chemical Physics* 123 (2005). PDF.

[11] Lorenz, Persson, et al. "Rubber Friction for Tire Tread Compound On Road Surfaces" *Journal of Physics: Condensed Matter* 25 (2013). PDF.

[12] Lorenz, B. *Contact Mechanics and Friction of Elastic Solids on Hard and Rough Substrates*. Diss. Forschungszentrum Jülich GmbH Zentralbibliothek. 2012. PDF.

[13] Nayak, P. “Some Aspects Of Surface Roughness Measurement.” *Wear* 26 (1973): 165-174

[14] Nguyen, Ramakrishna, et al. “Friction of Rubber with Surfaces Patterned with Rigid Spherical Asperities.” *Tribology Letters* 49.1 (2013): 135-144. PDF.

[15] Ma, Gao, Zhang, and Wu. “A Versatile Analytical Expression for the Inverse Abel Transform Applied to Experimental Data with Noise.” Applied Spectroscopy 62.2 (2008).

[16] Moore, Desmond F. *The Friction and Lubrication of Elastomer.* Oxford: Pergamon Press, 1972.

[17] Moore, Desmond F. *The Friction of Pneumatic tires.* Amsterdam: Elsivier Scientific Publishing Company, 1975.

[18] Multiscale Consulting. “Fourier Transformation of Surface Roughness.” Online Posting, YouTube, 28 Feb. 2014. Web. 23 Aug. 2013.

[19] Multiscale Consulting. “Contact Mechanics and Surface Roughness.” Online Posting. YouTube, 28 Feb 2014. Web. 26 Aug. 2013.

[20] Persson, B.N.J. “Theory of Rubber Friction and Contact Mechanics,” *Journal of Chemical Physics 115.8* (2001): 3840-3861. PDF.

[21] Persson, B.N.J. “Rubber Friction: Roll of the Flash Temperature,” *Journal of Physics: Condensed Matter* 18 (2006): 7789-7823. PDF.

[22] Persson, B.N.J. “On the Theory of Rubber Friction.” *Surface Science* 401 (1998): 445-454. PDF.

[23] Persson, B.N.J. “Rubber Friction and Tire Dynamics.” *Journal of Physics: Condensed Matter* 23, (2011). PDF.

[24] Persson, B.N.J. “Contact Mechanics for Randomly Rough Surface.” *Surface Science Reports* 61 (2006): 201-227. PDF.

[25] Persson, Tartaglino, et al. “Rubber Friction on Wet and Dry Road Surfaces: The Sealing Effect.” *Physical Review* B 71 (2005). PDF.

[26] Persson, Albohr, et al. “On the Nature of Surface Roughness With Application to Contact Mechanics, Sealing, Rubber Friction and Adhesion.” *Journal of Physics: Condensed Matter* 17 (2005) R1-R62. PDF.

[27] Pinnington, R.J. “Rubber Friction on Rough and Smooth Surfaces.” *Wear* 267 (2009): 1653-1664

[28] Savkoor, A.R. *Tribology and Tyre Traction on Dry and Wet Roads.* 1992

[29] Scaraggi, M., Putignano, C., and Carbone, G. “Elastic Contact of Rough Surfaces: A Simple Criterion to Make 2D Isotropic Roughness equal to 1D One.” *Wear* 297 (2013): 811-817.

[30] Technical Committee CEN/TC 227 “European Standard 13036-4. “Method for measurement of slip/skid resistance of surface – Part 4: The pendulum test.” 2009.

[31] Williams M L, Landel R F and Ferry J D. “The Temperature dependence of Relaxation Mechanisms in Amorphous Polymer and Other Glass-forming Liquids. *American Chemical Society Journal* 77 (1955) PDF.